Universidade de Aveiro Departamento de Engenharia Mecânica
2014

Paulo Sérgio Barros Julião

Electrolytic Cells for Plastic Waste Recycling

Células Electrolíticas para Reciclagem de Resíduos Plásticos

Universidade de Aveiro Departamento de Engenharia Mecânica
2014

Paulo Sérgio Barros Julião

Electrolytic Cells for Plastic Waste Recycling

Células Electrolíticas para Reciclagem de Resíduos Plásticos

Dissertação apresentada à Universidade de Aveiro para cumprimento dos requisitos necessários à obtenção do grau de Mestre em Sistemas Energéticos Sustentáveis, realizada sob a orientação científica do Prof. Doutor Duncan Paul Fagg, Equiparado a Professor Auxiliar do Departamento de Engenharia Mecânica da Universidade de Aveiro e do Prof. Doutor Jorge Ribeiro Frade, Professor Catedrático do Departamento de Engenharia de Materiais e Cerâmica da Universidade de Aveiro.

Para a melhor mãe que alguém podia ter.

o júri

presidente

Prof. Doutor Luís António da Cruz Tarelho
professor auxiliar do Departamento de Engenharia de Ambiente e Ordenamento da Universidade de Aveiro

Doutor Duncan Paul Fagg
investigador auxiliar do Departamento de Engenharia Mecânica da Universidade de Aveiro

Doutor Aleksey Yaremchenko
investigador principal do Departamento de Engenharia de Materiais e Cerâmica da Universidade de Aveiro

agradecimentos

Perante a natureza, não podemos negar que pessoas são feitas de outras pessoas e por isso, nós influenciamos os outros nas mais diversas maneiras e com os mais variados comportamentos e formas de estar na vida. Pessoas que por todo o mundo realizam os mais belos trabalhos, projectos e obras de arte, são no fundo também feitos de todos nós. Este trabalho não é excepção e foi portanto "feito" também por imensas pessoas que me ensinaram, apoiaram e fizeram de mim e deste trabalho o que somos hoje:
Sergey Mikhalev
Duncan Fagg
Pukazh Selvan
Nazani Narendar
Aliaksandr Shaula
Ana Daniela Brandão
Ricardo Beja
Carlos Almeida
Javi Garcia
Isabel Antunes
Tao Yang

palavras-chave

Céculas de combustível de óxido sólido, Ânodos de metal líquido, Diagramas de fase, Fusão congruente, Diagrama de Ellingham, Pressão de vapor

resumo

Este estudo incidiu sobre potenciais ânodos líquidos de ligas metálicas para células electrolíticas (do tipo SOFC) alimentadas por resíduos sólidos. Alguns sistemas de ânodos possíveis foram identificados através de um estudo detalhado de diagramas de fase. O sistema de óxidos metálicos PbO-Sb_2O_3 foi selecionado como uma possível liga metálica para esta aplicação. Este sistema foi sujeito a um estudo detalhado de pressão de vapor. Algumas células foram fabricadas para avaliar experimentalmente as propriedades electro-químicas deste sistema. Este trabalho revela imensas características que inesperadamente limitaram este estudo, tal como a incompatibilidade entre platina e a liga metálica escolhida. Uma segunda célula foi construída, desta vez usando um fio de rénio, prevenindo tal reacção. No entanto, o fio de rénio sublima sobre condições oxidantes (ar) e, perante um uso prolongado, o vidro selante e a liga metálica reagem entre si. Considerando todas estas incompatibilidades, um terceiro modelo de célula foi criado, ultrapassando alguns obstáculos e fornecendo alguma informação inicial relativa ao comportamento electro-químico. O presente trabalho mostra que vários parâmetros precisam precisam de ser abordados de modo a assegurar a compatibilidade dos materiais. Relativamente ao sistema PbO-Sb_2O_3, a elevada volatilidade de Sb_2O_3 foi uma grave limitação que só pode ser contornada através da aplicação de novos fios conectores, materiais e condições de selamento. No entanto, este projecto destaca outros potenciais sistemas que podem ser estudados, como $Pb_{11}Ge_3O_{17}$, Pb_3GeO_5, $Pb_5Ge_3O_{11}$, Bi_2CuO_4, Bi_2PdO_4, $Bi_{12}GeO_{20}$.

keywords

Solid Oxide Fuel Cells, Liquid Metal Anodes, Phase diagram, Congruent melt, Ellingham diagram, Vapor pressure

abstract

The current project assesses potential molten alloy anodes for Solid Oxide Fuel Cells (SOFC) running on solid waste. A detailed phase diagram study was performed to locate probable anode systems. The molten metal oxide system PbO-Sb_2O_3 was selected as a possible molten alloy anode for this application. A detailed vapour pressure study of this system was performed. Several cells were fabricated to experimentally assess the electrochemical properties of this system. The work reveals several unexpected limiting features such as the incompatibility between the platinum and the chosen alloy. A second cell was built, this time using rhenium wires instead, preventing such reaction. However, the rhenium wire sublimes under oxidizing conditions (air) and the sealing glass and the chosen alloy system react with each other under long term use. Considering all these issues, a third cell design was conceived, surpassing some obstacles and providing some initial information regarding the electrochemical behaviour. The current project shows that many parameters need to be taken into account to ensure materials compatibility. For the PbO-Sb_2O_3 system, the high volatility of Sb_2O_3 was a serious limitation that can only be addressed through the application of new contact wires or sealing materials and conditions. Nonetheless, the project highlights several other potential systems that can be considered, such as $Pb_{11}Ge_3O_{17}$, Pb_3GeO_5, $Pb_5Ge_3O_{11}$, Bi_2CuO_4, Bi_2PdO_4, $Bi_{12}GeO_{20}$.

Table of Contents

List of figures

List of Tables

Chapter 1 - Introduction

1.1 Framework

Energy is the capacity of a physical system to perform work. Some materials are able to store this potential energy, and are called fuels. The earth contains several kinds of fuels, and for the same unit of volume or mass, some fuels contain more energy than others. This propriety is called energy density, or, specific energy. Today, fossil fuels (coal, oil and natural gas) are the dominant worldwide suppliers of energy (Figure 1) and one of the reasons behind this is that these fuels offer the highest values of specific energy.

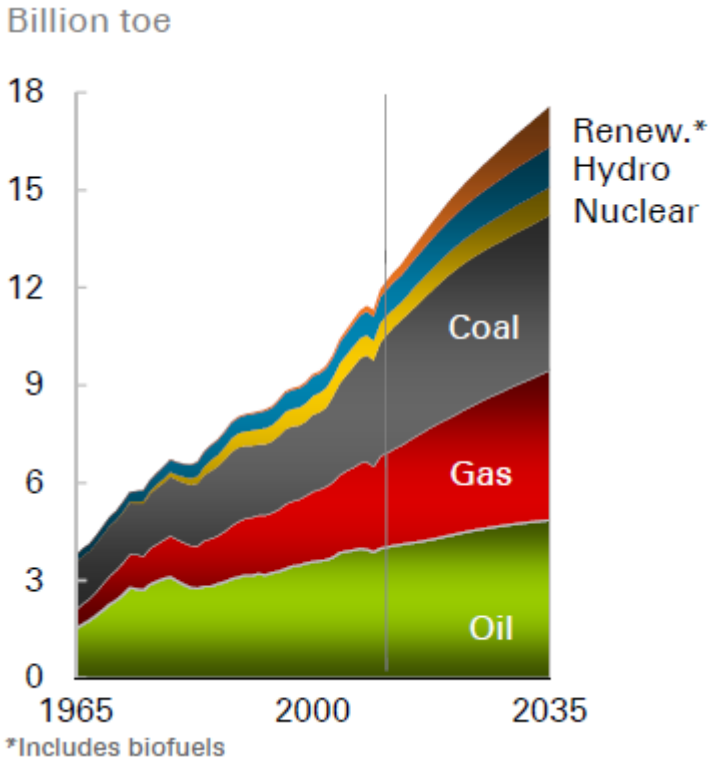

Figure 1 – World's consumption by fuel [1]

The formation time of fossil fuels is comparatively much longer than today's elevated rate of consumption. New alternatives to fight this issue such as renewable energy projects, have been studied, developed and implemented over the years. A renewable resource is, by definition, any natural resource that can replenish itself naturally over time. Unfortunately despite the fact that fossil fuels are continuously being formed in the planet, they are not considered renewable due to the large imbalance between their rate of usage and their rate of formation.

Most of the electricity supplied in the world today comes from burning fossil fuels in power plants to generate heat that is converted in electricity injected in the grid. The demand for electricity changes depending on both the seasons and the time of day. In order to fulfil the energy demand along with its variance, these utilities possess 3 kinds of plants: baseload, intermediate load and peak load. The base load plants work full time except in case of repairs or maintenance events. Intermediate load plants are cyclic and operate only during the day. While the peak load plants only run for short day time periods (between 2 to 3 hours usually) where the demand for electricity is higher.

In most of the renewable energy systems, the demand for electricity is fulfilled through energy storage, because most of these systems have intermittent operation. Aside of some exceptions like geothermal energy, typical renewables, such as wind power, solar and hydropower, depend on the weather conditions. For example, in Portugal, electricity production from renewable

sources increased from 58.3% (in 2012) to 61.7% (in 2013) due to the distinct meteorological conditions in each year [2].

There are several kinds of stored energy, but this study will focus in the use of chemical potential energy that subsequently can be converted into electrical kinetic energy. Analogously to the potential energy of a damned river that can be turned into kinetic energy when the dam opens the floodgates, a fuel cell can release its chemical energy by transforming this energy into electrical energy through a reduction-oxidation reaction. The reduction-oxidation reactions within fuel cells serve the purpose of chemical energy release, generating a flow of electrical current upon the electrochemical oxidation of fuels. The current work aims extend current knowledge by developing materials for a specialised type of solid oxide fuel cell that can utilise waste plastics as the fuel source.

1.2 Solid Oxide Fuel Cells

The Solid oxide fuel cell (SOFC) is a promising technology that provides efficient and clean electrical energy production for wide range of applications. This technology consists of an effective process to produce electricity from chemical components due to a high conversion efficiency that maximizes environmental acceptability. A fuel cell consists of three main parts: two electrodes (an anode and a cathode) and one electrolyte. The electrolyte component is a solid oxide ceramic membrane, which, in the current case, is that of an oxide-ion conductor.

Supplied from external sources, the fuel (e.g. H_2, CO, CH_4) and the oxidant (e.g. air) are introduced to the anode and cathode sides respectively (Figure 2). Electrochemical reduction of oxygen occurs at the cathode with the consumption of electrons to produce an oxide-ion O^{2-}. These ions conduct through the electrolyte to the anode, where they electrochemically oxidize the fuel, liberating electrons. The electrons flow through an external circuit where they can perform work.

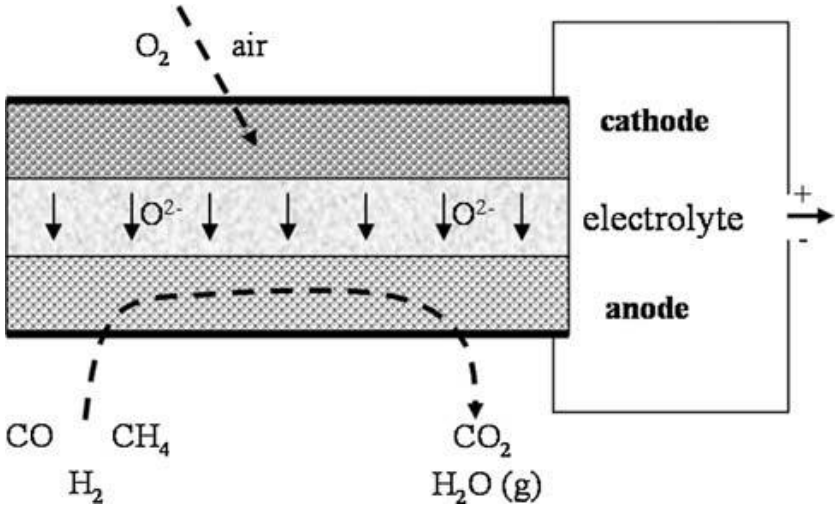

Figure 2 – SOFC chemical scheme [3]

SOFCs have generated particular interest due to their high operation temperature and their solid state nature. The solid ceramic design allows utilization of the electrode or the electrolyte as part of the structural members of the cell to prove a compact, inert and robust construction that can also eliminate problems of electrolyte migration and containment that plague alternative fuel cells designs, such as, molten carbonate fuel cells or proton exchange membrane fuel cells (PEM). The high operating temperature produces high-quality heat for energy conversion or other uses, stimulates rapid kinetics with non-precious metals and allows internal reforming of gaseous fuel within the cells. These latter features correspond to the main advantages offered by SOFC over that of the lower temperature technology of PEM fuel cells. In spite of these positive attributes, the ability to form functional devices is controlled by several rigorous requirements of the ceramic

components. Stability during oxidation or reduction events, chemical and thermal compatibility of each of the cell components, as well as the tailoring of proper electronic and ionic conductivity in the electrodes and electrolyte are some of the special materials engineering demands of this technology [4].

1.3 SOFC materials of the components

1.3.1 Solid electrolytes

As stated previously, the electrode must conduct oxide ion from the cathode to the anode, whilst being an insulator of electronic conductivity. The electrolyte must, therefore, possess a high oxide ion conductivity, very low electronic conductivity, compatible thermal expansion with the other cell components (like the electrodes), chemical stability in contact with the two electrodes as well as low cost. Currently the most used material is Yttria Stabilized Zirconia (8 YSZ, with 8% of yttrium (III) oxide, also known as yttria). The yttria (Y_2O_3) doping stabilizes the cubic fluorite structural phase and increases conductivity (as shown in Figure 3) by increasing the concentration of oxygen vacancies. At 1000°C, the conductivity reaches its maximum value when the mole percentage of yttria is around 8% and beyond this molar percentage further structural point defects lead to a reduction in oxide ion mobility, decreasing the conductivity. In the same way as zirconia is doped with yttria in order to increase ionic conduction; other dopant oxides like scandium oxide have also been suggested to increase conductivity to even higher values [5].

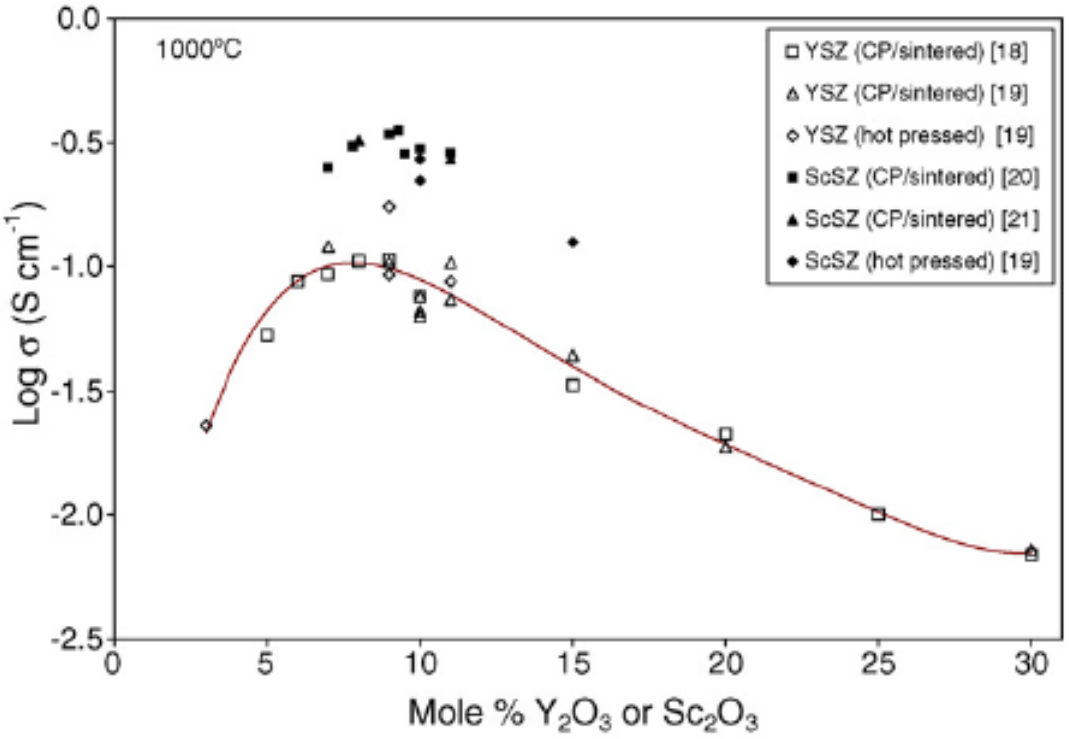

Figure 3 – Conductivity of yttria and Scandia stabilized zirconia in air at 1000°C [5]

This concept of doping materials to alter their proprieties through modifications of their defect chemistry is applied to other materials besides YSZ and ScSZ. Several substances are being synthesized and studied, for instance: lanthanum gallate with the strontium doping on the A site of the perovskite and magnesium on the B site (LSGM) or even ytterbia-stabilized zirconia (YbSZ). Figure 4 contains data from multiple studies over the years in this subject and illustrates the ionic conductivity of several materials along with the temperature [6].

Several materials contain several advantages and disadvantages. As shown, scandia stabilized zirconia has higher conductivity when compared to the widely used YSZ, it has also good

stability in oxidizing and reducing environments with even better long-term stability than YSZ. On the other hand, and despite the fact that both rare earth elements exist in similar abundance, scandia is much more expensive than yttria. Some materials show even higher conductivity than YSZ and ScSZ, like Gadolinia-Doped Ceria (GDC), also called Cerium Gadolinium Oxide (CGO). However, at low oxygen partial pressure it shows significant electronic conduction, furthermore it has lower mechanical stability and the price and availability of gadolinium limits the widespread synthesis of these compounds. LSGM electrolytes shown in Figure 4 possess high ionic conductivity at low temperatures, but those electrolytes demonstrate low phase stability, as well as the risk of the evaporation of the gallium element at low oxygen partial pressures. The LSGM electrolytes are also incompatible with nickel oxide "NiO", which is generally applied to the anode of the cell, and, analogous to the GDC electrolytes, the LSGM are limited by the price and availability of gallium [4].

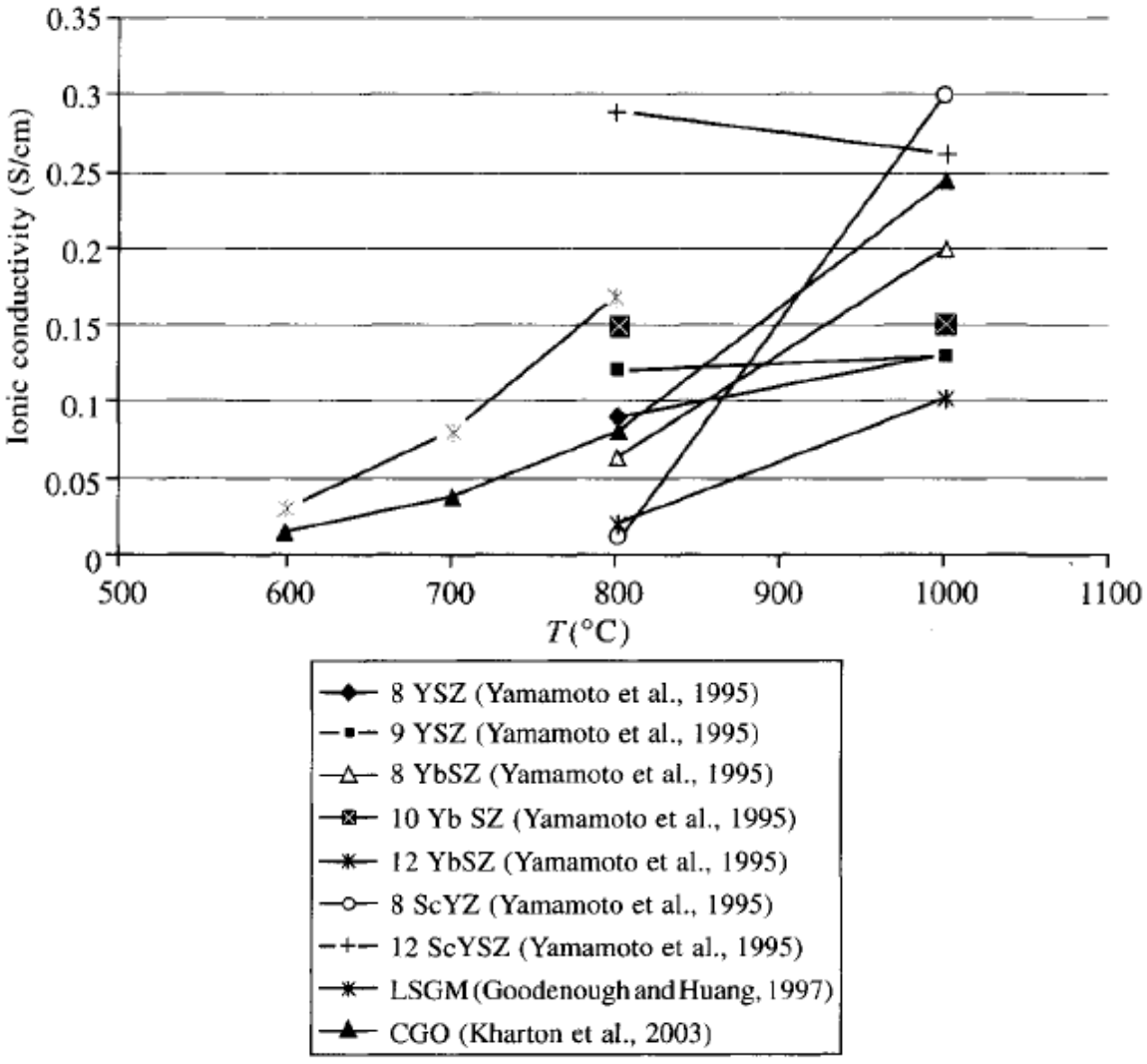

Figure 4 – Ionic conductivity studies of different oxide ion conducting electrolytes [6]

Other important factor is the electrolyte thickness, because it directly affects the total cell performance due to increasing the associated potential losses attributable to the electrolyte ohmic resistance at any fixed current. This factor is shown graphically in (Figure 5) [7] which plots the temperature dependence of ohmic polarization loss for different electrolyte thickness. It can be observed that both conductivity (e.g. the lower conductivity of YSZ in comparison to LSGM) and

thickness can cause the ohmic polarization losses to exceed target values (labeled as “maximum”). This factor becomes more severe on decreasing temperature and leads to the requirement of thinner and thinner electrolytes to continue to remain in the target range.

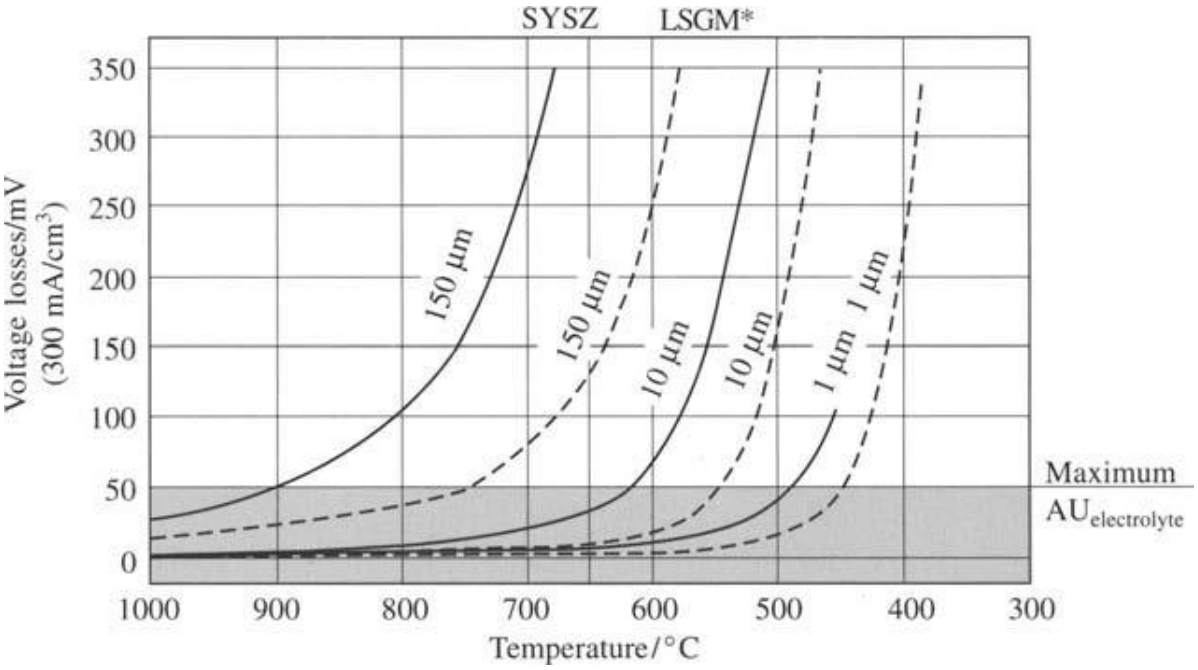

Figure 5 – Temperature dependence of voltage losses as function of YSZ and LSGM electrolytes thickness [7]

1.3.2 Electrodes

The electrodes of a fuel cell have many requirements, such as high electronic and ionic conductivity and compatible thermal expansions with all other cell components. In addiction they must provide chemical stability, resistance to thermal cycling and high catalytic activity for the respective gas phase reaction.

1.3.2.1 Cathodes

A composite material formed from YSZ and perovskite $LaMnO_3$ doped with Strontium (LSM) is the most common type of cathode material used in standard SOFCs. The general formula of the perovskite-type oxide is ABO_3 in which the A-site cation is a mixture of rare and alkaline earths (like La and Sr, Ca or Ba) while the B-site contains a multivalent transition metal (like Mn, Fe, Co or Ni). A-site cations are larger and arranged in twelve fold coordination with oxygen ions. On the other hand, the B-site cations are less voluminous and are arranged in six fold coordination with oxygen ions. The multivalent nature of the transition metal (Figure 6) normally provides electronic conductivity and this may be enhanced with increasing oxygen partial pressure or by dopant strategies, such as the presence of Sr. The ionic conductivity in this composite material is primarily provided by the presence of YSZ as a secondary electrode component. In order to tailor both electrical conductivity and electro catalytic performance many perovskite cathodes involve more complex doping strategies on both cation sites to provide high levels of both electronic and ionic conductivity [8].

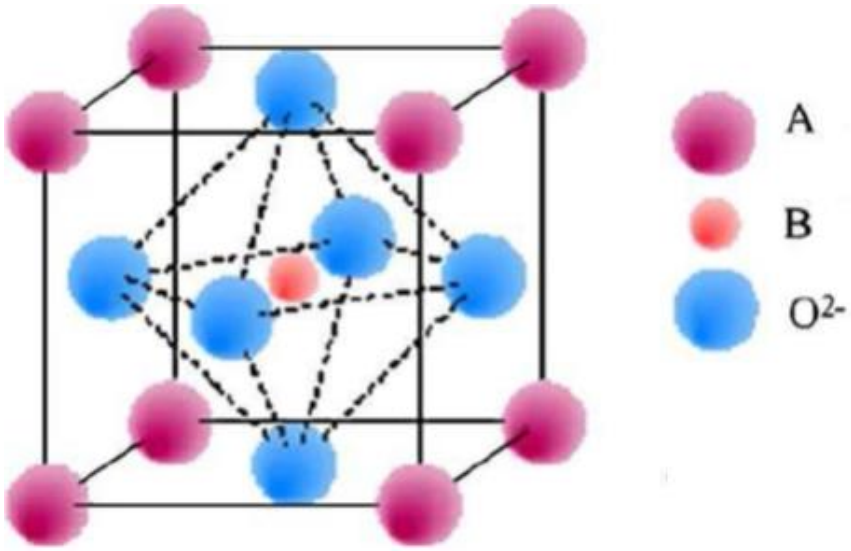

Figure 6 – Unit cell of the ABO_3 perovskite structure [9]

The already mentioned perovskite lanthanum magnetite-based cathode is commonly doped with strontium because its size matches with lanthanum. In this specific case the acceptor dopant Sr increases the electron-hole concentration and improves the electrical conductivity (that increases approximately linearly along with the Sr concentration up to a maximum around 50% molar ratio). Other popular cathode materials are strontium doped lanthanide (La, Pr, Gd etc.) cobalt ferrite (LSCF) which offers a high mixed conductivity of both ionic and electronic charge carriers. In Figure 7 it is seen the cathode performance variation along with different percentages of iron and cobalt content in the compound LSCF, where the lanthanide was Pr.

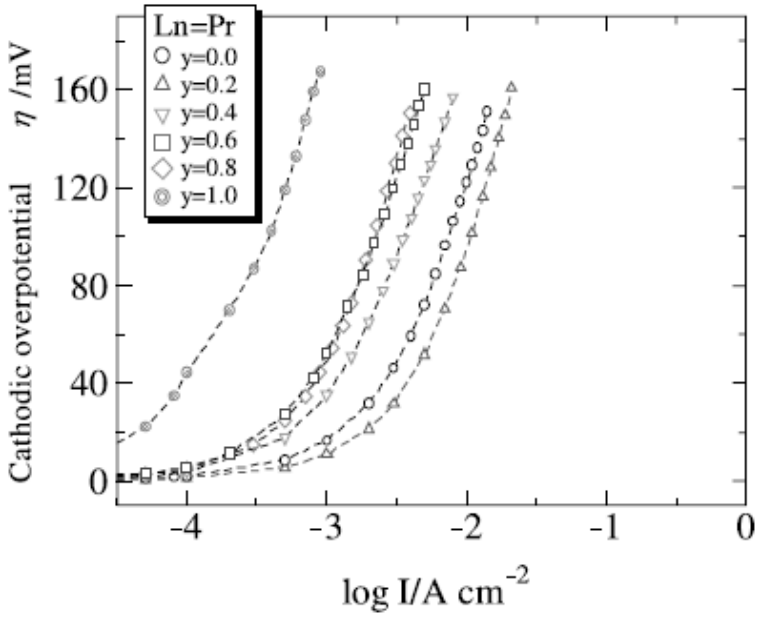

Figure 7 – Polarization behavior of cathodes at 700°C for different Co/Fe ratios ins LSCF, where the lanthanide is that of Pr [10]

Although LSM is usually stable under oxidizing conditions, it dissociates in highly reducing conditions and its electrical proprieties are not good enough to be applied at scenarios with

operation temperatures below 800°C. This is mainly due limitations in oxide ion transportation. As mentioned before, the existence of mixed ionic and electronic conductivity is a very important aspect to consider in cathodes materials [9].

Polarization losses usually are decreased through the proper composition choice (to improve the oxygen exchange and diffusion kinetics), and by microstructure optimization (to extend the triple phase boundaries at which the oxygen reduction reaction can occur). The triple phase boundary length is related to the activation polarization. In other words, microstructural and compositional tailoring aim to maximize this length to lower the activation polarization losses. The activation polarization is the quantification of the retarding factors inherent part of the relative kinetics of the electrochemical reaction within the cell. In this case, the activation polarization describes the reduction reaction of oxygen at the cathode surface, its conversion into oxide-ions and the passage of these oxide ions into the electrolyte.

1.3.2.2 Anodes

As mentioned before, there are some strict requirements the materials of the anode must fulfill. Typically a composite material is used that consists of nickel metal and a ceramic YSZ oxide ion conducting phase. This combination of a CERamic and METal is called a cermet. Nickel metal provides electronic conductivity, while YSZ provides the oxide-ion conduction. Nickel is chemically stable in towards the YSZ (they are immiscible in each other and non-reactive over a very wide temperature), and its cost is relatively low. All of these factors make the porous Ni-YSZ cermet the most common anode material utilized in SOFC. When compared to nickel metal, copper would provide a cheaper solution with some advantages as well, such as higher tolerance to carbon deposition and sulfur impurities; on the other hand, it is not stable at SOFC operating conditions nor offers sufficient catalytic performance [11]. Nickel has lower conductivity, but is stable at the cell operating conditions and offers one of the highest catalytic performances for hydrocarbon fuel oxidation. The most common concentration of Nickel in the YSZ is around 40 to 45 vol% in order to achieve percolation (Figure 8).

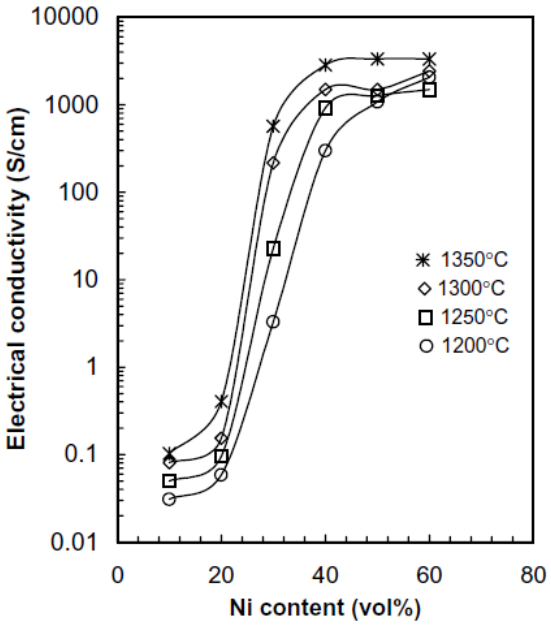

Figure 8 – Variation of electrical conductivity measured at 1000°C as a function of nickel concentration in Ni/YSZ cermet fired at different temperatures [12]

Another important parameter related to the performance of the anode cermet is that of microstructure. To study this behavior, the conductivity values at a certain temperature have been

assessed while varying the content of a coarse and fine YSZ (Figure 9). Besides increasing the conductivity, the coarse particles of YSZ have their influence in several other useful characteristics, such as, the control of thermal expansion, the prevention of significant shrinkage in the anode layer, the inhibition Ni agglomeration and preservation of porosity formation within the structure [11].

For low temperature solid oxide fuel cells, the rare earth doped CeO_2 material in combination with Ni has also been suggested as a potential anode due to its potential additional electrocatalytic activity, enabling the direct oxidation of low hydrocarbon gases; and its higher ionic conductivity at lower temperatures. However, its mechanical stability in reducing environments has been shown to be inferior when compared to the Ni-YSZ cermet material. Many other single phase materials have been studied as well, for example lanthanum chromite (with good thermal and chemical stability, but poor mechanical response and high chemical expansion in reducing atmosphere), or mixed conducting $SrTiO_3$ based materials (with n-type of in reducing atmospheres, however, with inferior electrochemical performance when compared to the aforementioned Ni-Cermet anodes) are just some examples of the alternative anode materials whose proprieties have been investigated [12].

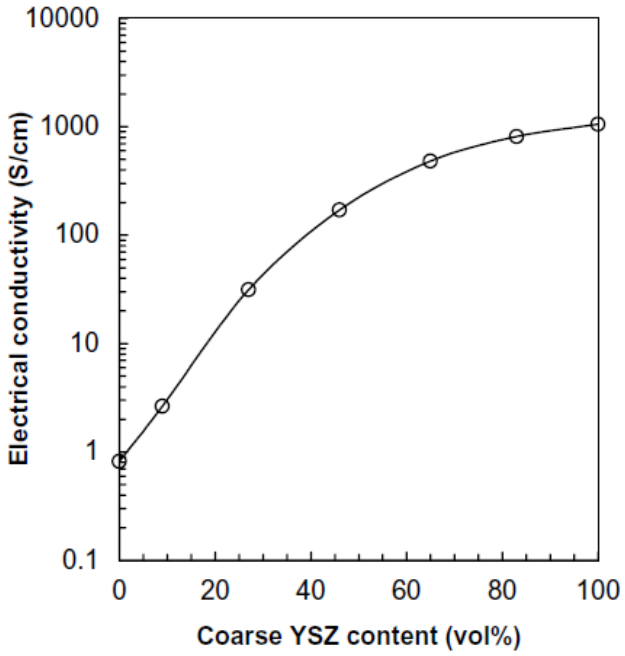

Figure 9 – Electrical conductivity measured at 1000°C of Ni/YSZ cermet containing both coarse and fine YSZ particles as a function of coarse YSZ content of total YSZ [12].

1.3.2.2.1 Liquid metal anode SOFCs – application to solid fuels

Plastic waste is a major constituent of municipal solid waste (Figure 10), arising from the packaging, films, covers, bags, containers etc. widely used in daily life [13]. To date plastic recycling has been dominated by mechanical recycling, where plastic waste is recycled without breaking the material's chemical structure by grinding, shredding or melting [14]. It is mainly applied to thermoplastics and its nature can be primary, which entails closed loop recycling where the new products have equivalent properties to the former ones or secondary, where recovered plastic must be put into other applications due to of the downgrading of properties **[15]**. Tertiary (or chemical) recycling, where the plastic materials are recycled back to their precursors from which other products may be formed, has been performed only to a lesser extent (only 0.3% (0.07Mt) of the total plastic waste in Europe in the year 2008, in comparison to mechanical recycling at 21.3% (5.3 Mt) [16]. The current project aims to use waste plastic as a valuable fuel in liquid metal anode SOFCs. A schematic of the proposed liquid metal anode SOFC is shown in Figure 11.

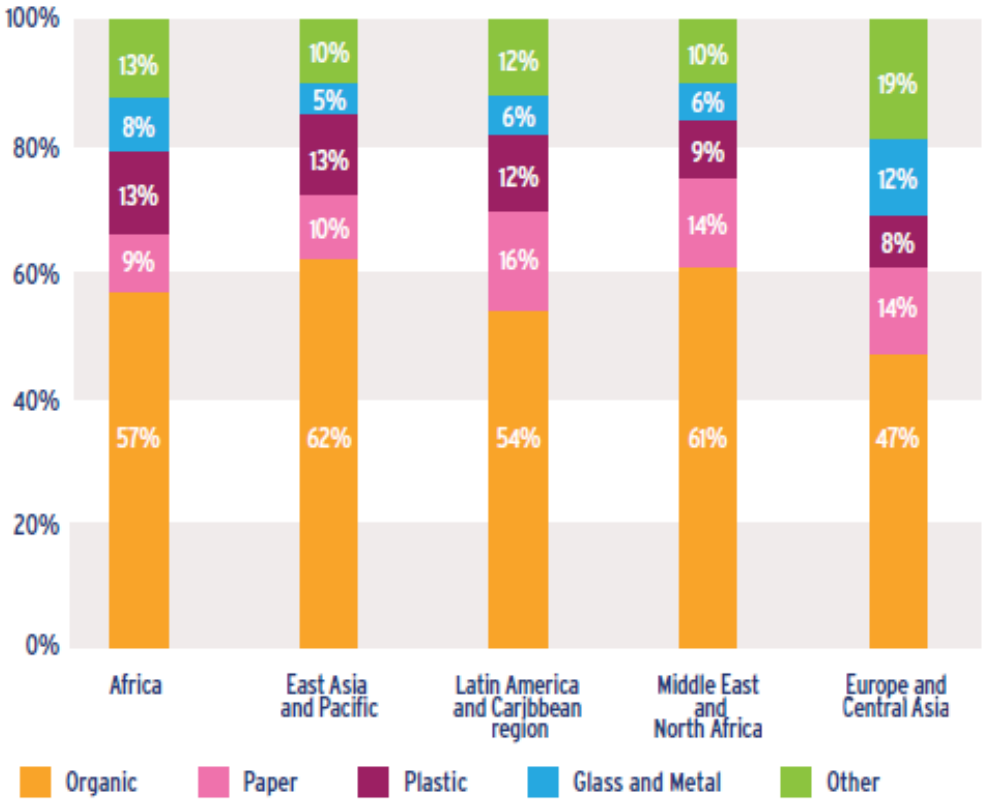

Figure 10 – Municipal solid waste composition by region in 2012 [17]

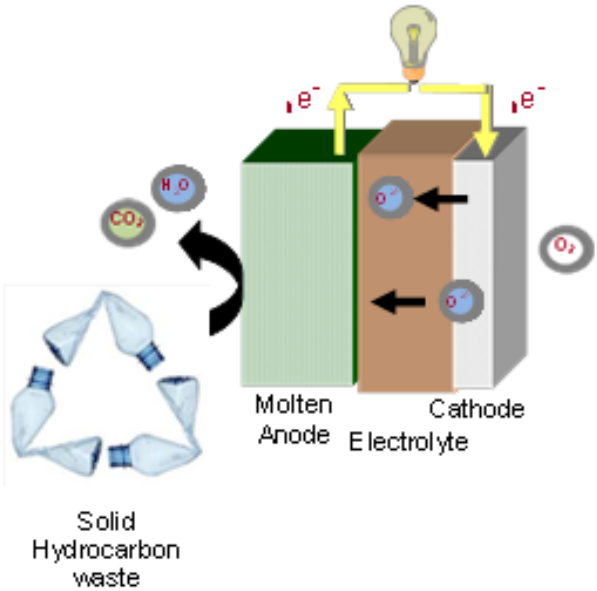

Figure 11 – SOFC's liquid metal anode schematic

Unfortunately, the conventional SOFC is not equipped to cope with solid waste, as typical electrode materials, such as Ni-cermets do not offer sufficient contact area for its electrochemical

oxidation. Thus, recent work has looked into the use of molten metals as alternative anodes in these devices. The concept of liquid metal anodes has only been demonstrated in a handful of articles of cells operating in the fuel cell mode [18]-[20]. Due to this novelty, there is a notable lack of information about the factors that can limit the performance of liquid metal electrodes and, thus, how they should be improved. Fledgling studies on a range of pure metals (such as Bi, Ag, Sn, Sb, Pb) have suggested the following, basic, criteria for electrode functionality.

Primarily, the molten metal electrode must offer lower oxygen affinity than carbon to offer the required driving force for carbon oxidation. Secondly, the theoretical open circuit potential of such anodes in the presence of carbonaceous waste would be determined by the thermodynamics of the carbon oxidation reaction; nonetheless, one can only obtain this potential if the rate of carbon oxidation is more rapid than the rate of oxygen transfer through the electrolyte. This requirement implies that the molten metal anodes should also possess the properties of high catalytic activity and fast oxygen permeation to guarantee unhindered oxidation of the carbonaceous waste. In this respect, the performance of the most commonly used liquid anode material, Sn, is shown to be severely limited by its poor oxygen transport. The oxidised product, SnO_2, is a solid at the working temperatures, leading to the formation of a dense and impermeable SnO_2 coating on the electrolyte surface which debilitates performance. Once this layer has formed, further oxidation of Sn cannot occur due to the negligible oxygen transport through the SnO_2 layer and the low solubility of oxygen in molten Sn [18]. Two alternative solutions have been proposed to circumvent this problem. Firstly, a M/MOx system can be used where the formed metal oxide MOx offers oxide-ion conductivity, an example of this approach is the use of the Bi/Bi_2O_3 system. The second approach is to use a system where the formed oxide is a liquid at the working temperature, an example of this type of system is that of Sb/Sb_2O_3 [18]. In a new progression, the use of alloys may offer many advantages with respect to tailoring of the desired properties, for example, tailoring of oxidation potentials, melting temperatures and, most importantly, the formation of binary or ternary oxide phases that are in the liquid state at the working temperature. Only one previous investigation has been performed on alloy melts as potential anodes to date [20]. Thus, the novelty of the current project is high.

1.3.2.2.2 Molten alloy anodes advantages (natural convection, lower operation temperature and an additional degree of freedom in materials choice)

One of the main focuses of this work will be the study of the molten alloy anode characteristics applied to the SOFC. The biggest of the advantages of having a molten alloy anode rather than a melt of a single metal is to manage to control subsequent proprieties, such as, oxidation potentials, melting temperature and the formation of binary or ternary oxide phases that are in the liquid state at the working temperature, solely by manipulating alloy composition.

Furthermore, when the oxide system is molten, the oxide density is inferior to the one in pure metal state; this fact enables the usage of natural convection. Once the oxide is reduced by the fuel, its density will increase, and if the electrolyte is located below, the gravitational force will help the metal to meet the electrolyte surface so that it can be oxidized again. When the metal becomes oxidized once more, its density will decrease again, leading to its natural ascendance due to density decrease, and so on... In this small cycle all convection is natural, because there are no external forces besides gravity, thus, there is no requirement of external power usage to achieve this movement.

For some metals, the oxide formation decreases its melting point, lowering the required operational temperature to keep the anodic environment fluid (in this way, the cell's operation energy demand is lowered). The formation of mixed oxides by the use of metal alloys may offer reduced melting temperatures and/or a lower vapor pressure than the parent pure metal oxides allowing operation at lower temperatures and/or offering higher stability. Besides all of these advantages, the use of molten alloys as anodes provides an additional degree of freedom in the materials choosing process [21].

The chosen metal and corresponding metal oxide should be liquid at the cell operating temperature and will have to fulfill some other requirements discussed in the next chapter of the

present work that carefully explains the methodology and criteria with which appropriate materials can be chosen.

Chapter 2 - Methodology

The present work aims to find pairs of metal oxides to form a high performing liquid anode for the current, plastic fuelled, SOF device. Several criteria are suggested in order to select the best metals for the task. Firstly selection starts with elements that present a less negative Gibbs oxidation energy when directly compared with the carbon oxidation reaction. Upon cell operation, oxide-ions are passed from electrolyte into the anode metal melt (M) leading to the oxidation of the liquid anode (MO). For the device to continue to operate it is important that the carbon oxidation reaction (equation 1) is more spontaneous than the metal oxidation reaction (equation 2). In this way formation of CO_2 will occur in the anodic environment as the carbonaceous fuel is oxidized, while the oxidized liquid metal anode is instantaneously reduced and can return to the anode/electrolyte interface to be re-oxidized. Such a process will keep a flux of O^{2-} ions passing through the electrolyte, to continuously oxidize the fuel and produce a constant flow of electrons to the external circuit where they are available to perform work. To assess the respective Gibbs energies of each metal, the corresponding Ellingham diagrams were consulted [22]. From this first criterion the following elements were selected: Nickel (Ni), Copper (Cu), Zinc (Zn), Palladium (Pd), Silver (Ag), Cadmium (Cd), Germanium (Ge), Arsenic (As), Antimony (Sb), Tin (Sn), Lead (Pb), Bismuth (Bi). Vanadium (V), Tungsten (W) and Molybdenum (Mo) were added to the analysis (even if some of these oxidation reaction contain higher Gibbs energy values than the carbon reaction at the operation temperature), because those elements may be useful to form oxides with lower melting point than the respective pure metals.

$$2MO + C -> 2M + CO_2 \quad (1)\ [21]$$

$$M + O^{2-} -> MO + 2e^- \quad (2)\ [21]$$

(Where “M” stands for the generic metal element)

For these elements it was examined what are the possible oxidation states for each one of those elements and once those were selected (Ag_2O, As_2O_3, As_2O_5, Bi_2O_3, CdO, CuO, Cu_2O, GeO, GeO_2, MoO_2, MoO_3, NiO, Ni_2O_3, PbO, PbO_2, Pb_3O_4, PdO, Sb_2O_3, Sb_2O_4, Sb_2O_5, SnO, SnO_2, VO, VO_2, V_2O_3, V_2O_5, WO_2, WO_3, W_2O_3, W_2O_5, ZnO), a table to define all the possible oxide pair combinations was created.

Factsage [23] software was used to obtain the phase diagrams related to all the possible oxide combinations. However, some of the phase diagrams obtained by the software were not available due to lacking information in the program database. Thus, the software acquired information was combined with phase diagrams from literature bibliography [24]. From the identified systems the aim was to assess which metal pairs offered oxide compositions which would be liquid at the working temperature of the experiment. The temperature of 1000°C was chosen for this criterion. With reference to the Factsage software, only some of metal oxide combinations were shown to offer potentially usable oxide pairs (As_2O_3-Cu_2O, PbO-CuO, PbO-GeO, PbO_2-GeO_2, Pb_3O_4-GeO_2). Nonetheless, the information provided in the Factsage database was shown to be very limited. The available phase diagrams only provided information at partial temperature ranges that prevented important conclusions at lower temperatures, for example potential segregations of the anode compounds during the cooling process.

Further literature phase diagrams were also sourced to try to compensate the lack of data present in the Factsage software. In the 12 volumes of “Phase Diagrams for Ceramists” [24], 54 diagrams were found and from those, six elimination criteria were applied until the chosen pair of oxides could be reduced to only a few candidates (Table 1). All the applied criteria definition in this elimination process is carefully explained in the respective topic. From the first to the sixth, the criteria are defined respectively as i) melting point, ii) potential operation range, iii) congruent melting, iv) comparison of phase diagrams of oxides and pure metals, v) thermodynamic analysis of oxidation reactions and vi) monetary factor.

Table 1 – Analysed oxide systems

Volume	Fulfilled criteria			
	1st ,2nd and 3rd criteria	4th criteria	5th criteria	6th criteria
1	Bi_2O_3-PbO			
	Bi_2O_3-Sb_2O_3			
	Bi_2O_3-SnO_2			
	Bi_2O_3-ZnO	Bi_2O_3-ZnO		
	PbO-Sb_2O_4			
	PbO-Sb_2O_5			
	PbO-SnO_2			
2	(none)	(none)		
3	Bi_2O_3-NiO			
	PbO-Sb_2O_3	PbO-Sb_2O_3	PbO-Sb_2O_3	PbO-Sb_2O_3
	PbO-SnO			
	PbO-WO_3	PbO-WO_3		
4	Bi_2O_3-MoO_3	Bi_2O_3-MoO_3		
	GeO_2-PbO	GeO_2-PbO	GeO_2-PbO	
6	As_2O_3-PbO			
	Bi_2O_3-CuO	Bi_2O_3-CuO	Bi_2O_3-CuO	
	Bi_2O_3-PdO	Bi_2O_3-PdO	Bi_2O_3-PdO	
	Cu_2O-GeO_2			
	Cu_2O-PbO			
	MoO_3-ZnO			
	PbO-ZnO			
	Sb_2O_3-V_2O_5	Sb_2O_3-V_2O_5		
8	(none)	(none)		
11	Bi_2O_3-CdO			
	Bi_2O_3-GeO_2	Bi_2O_3-GeO_2	Bi_2O_3-GeO_2	
	Bi_2O_3-V_2O_5	Bi_2O_3-V_2O_5		
	PbO-V_2O_5			
12	As_2O_5-PbO	As_2O_5-PbO		

2.1 Melting point, operation gap and congruent melting (1st, 2nd and 3rd chosen criteria)

From the 54 total diagrams found in the 12 volumes (of the phase diagrams bibliography) only 26 binary metal oxide systems had liquid phases at temperatures inferior to 1000 °C and with a molar percentage width for existence of molten phases at 1000°C that was greater than 5%. These 26 diagrams were then selected and observed again in order to be tested for the next criteria.

It would also be beneficial if the oxide systems offered compositions that melted congruently. This was deemed necessary to prevent the segregation of formed oxide phases on cooling, so as to enable the realization of several experiments involving thermal cycling. Moreover, the oxides should, preferentially form a single molten oxide composition rather than a two phase mixture containing both molten and solid oxide phases. Due to this criterion, some of the phase diagrams were discarded directly because they did not fulfill these conditions, but others were discarded because they do not offer a sufficiently wide compositional range in the molten state or that the represented variation does not contain compositions of congruent melting. Additional systems were also discarded because of lack of available literature information.

2.2 Oxides and pure metals comparison (fourth criterion of choice)

Next, a fourth criterion was verified which consisted of the direct comparison between both oxide and pure metal phase diagrams in the very same elementary proportions. For instance, in the

As_2O_5-PbO system (Figure 12*)* it is possible to notice that the $Pb_8As_2O_{13}$ compound will melt at 865 °C (which is inferior to the operation temperature of 1000 °C). Directly comparing the oxide phase diagram with the pure metal phase diagram of these two metals (Arsenic and Lead) in the same compound proportions (since it is $Pb_8As_2O_{13}$, this leads to a proportion of 20% Arsenic), it is then intended to ascertain if there is liquid phase in a 20% Arsenic at any temperature lower than 1000°C. Once the proper pure metal phase diagram was not found in an online search, the FactSage software was then used to complete the information related to the missing diagrams that could not be obtained by the bibliography.

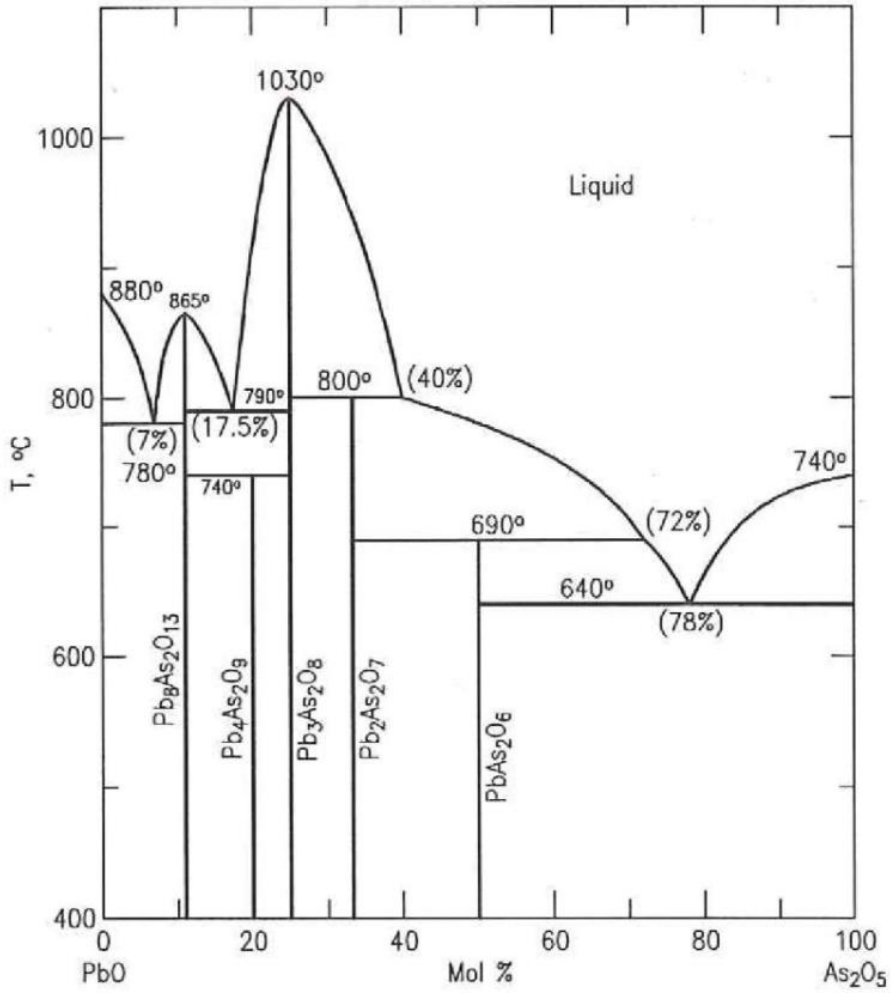

Figure 12 - As_2O_5-PbO phase diagram [24]

As it is seen by Figure 13, it is apparently possible to obtain a completely liquid phase at a temperature lower than 1000 °C in a 20% molar percentage of Arsenic. This means the Arsenic-Lead system is able to be tested in the next step criteria. This very same train of thought related to this criterion was applied to all of the phase diagrams, eliminating this way the PbO-WO_3, Bi_2O_3-MoO_3 and Sb_2O_3-V_2O_5 systems, as well as the $Bi_4V_2O_{11}$ and $BiVO_4$ substances present in the Bi_2O_3-V_2O_5 diagram.

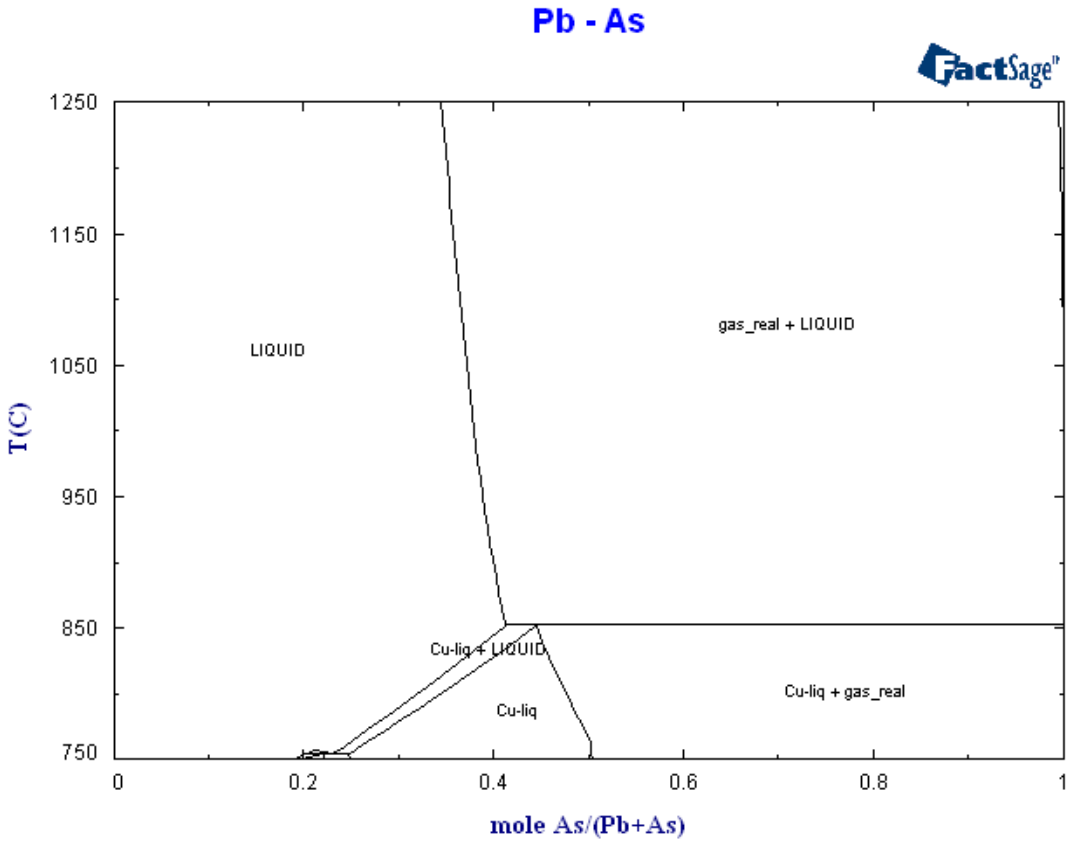

Figure 13 - As-Pb phase diagram [23]

2.3 Ellingham diagram analysis (fifth criterion of choice)

A fifth criterion was used to forecast the alloy oxides behavior. The oxidation reactions Gibbs energies related to the 8 remaining oxide pairs were then compared by use of the respective Ellingham diagrams [22]. This criterion could eliminate some of the systems in which the pure metals did not offer a lower oxygen affinity than carbon (for a temperature of 1000 °C).

Some systems can be retained when the values of Gibbs energy of one metal component is far less negative in comparison with the Gibbs energy related to the carbon oxidation reaction. In other words, the Gibbs energy difference between one of the metals and the carbon oxidation reaction must be significantly higher for the metal which possesses the least negative Gibbs energy. An example of this event is the Ellingham diagram for the oxidation reactions of Vanadium and Bismuth, where the low oxygen affinity of bismuth may compensate for the higher oxygen affinity of vanadium (Figure 14).

None of the diagrams were discarded because of failing completely this fifth criterion, however, the substances $Bi_{12}V_2O_{23}$ and $Bi_8V_2O_{17}$ of the oxides pair Bi_2O_3-V_2O_5 have higher chances of having oxidation Gibbs energies superior to the carbon oxidation Gibbs energy (at a 1000 °C) due to their higher concentration of vanadium.

As for the As_2O_5-PbO pair, this system was discarded due to lack of information in the Arsenic Ellingham diagram and also its toxicity. Except for these two pairs (As_2O_5-PbO and Bi_2O_3-V_2O_5), all the other oxide systems fit in the imposed oxygen affinity criteria.

Hereupon, the compounds that apparently correspond to the five previous criteria to compose the liquid anode of the electrochemical cell are: $PbSb_2O_4$, $Pb_{11}Ge_3O_{17}$, Pb_3GeO_5, $Pb_5Ge_3O_{11}$, Bi_2CuO_4, Bi_2PdO_4 e $Bi_{12}GeO_{20}$.

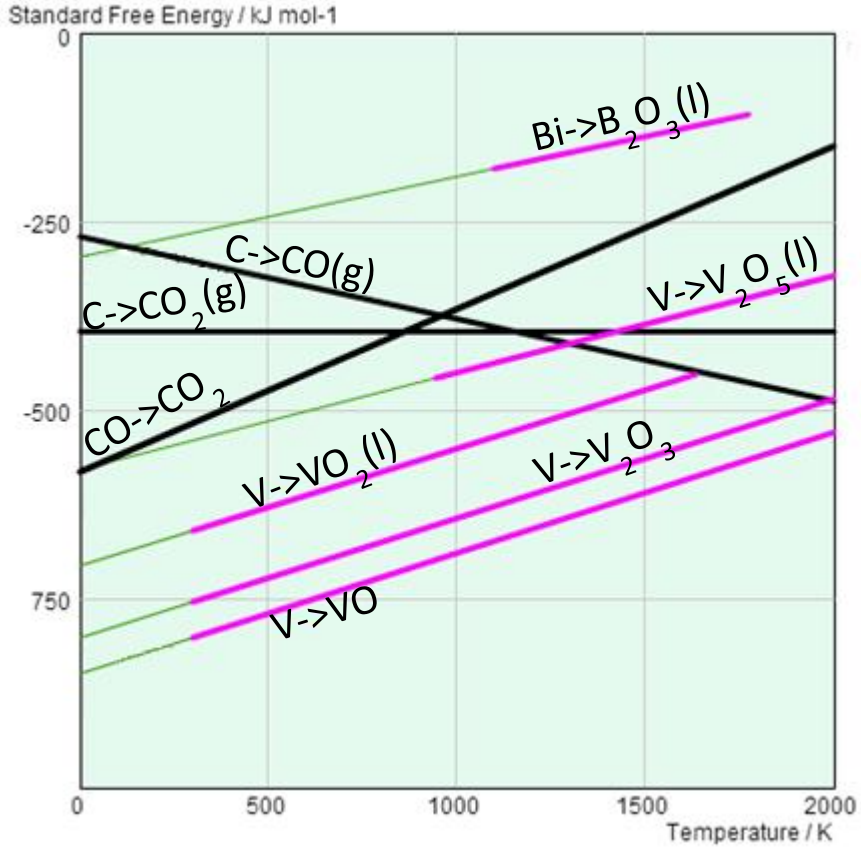

Figure 14 – Ellingham diagram of Vanadium, Bismuth and Carbon oxidation reactions [22]

2.4 Monetary factor (sixth criterion of choice)

The prices of the 6 oxides required to obtain the 7 previously indicated compounds where consulted in the web-site of the chemical company "Sigma-Aldrich" [25], in their proper proportions to form aforementioned substances.

2.4.1 Respective oxide amount calculation for the anodic substance

This part of the report explains how the correct proportions were determined to form 100g of each one of the 7 substances indicated in the previous section. To synthesize each one of the compounds it is needed to mix the oxide components in the correct ratio. As an example (A)GeO_2 + (B)PbO = (100g)$Pb_{11}Ge_3O_{17}$ the compound $Pb_{11}Ge_3O_{17}$ is formed by the following ration of lead and germanium oxides:

$$Pb_{11}Ge_3O_{17} = 11.PbO + 3.GeO_2 \quad (3)$$

For this molar ratio, in each 100g of $Pb_{11}Ge_3O_{17}$, 78.571g will be from GeO_2 and 21.429g will be from PbO. The same logic was analogously applied for all the remaining substances. Table 2 records all the calculated proportions of each of the 7 possible oxide compounds.

Once all of the oxide proportions were calculated, the costs evaluation step took place in order to find the cheapest compound to synthesize.

Table 2 – Oxides proportion to produce g of compound

Compound	**Oxide quantities to synthesize 100g of the compound**	
$PbO.Sb_2O_3$	50g of PbO	50g of Sb_2O_3
$Pb_{11}Ge_3O_{17}$	78.571g of PbO	21.429g of GeO_2
Pb_3GeO_5	75g of PbO	25g of GeO_2
$Pb_5Ge_3O_{11}$	62.5g of PbO	37.5g of GeO_2
Bi_2CuO_4	50g of Bi_2O_3	50g of CuO
Bi_2PdO_4	50g of Bi_2O_3	50g of PdO
$Bi_{12}GeO_{20}$	92.31g of Bi_2O_3	7.69g of GeO_2

2.4.2 Simulation of costs

The oxides needed to synthesize the substances are: PbO, Sb_2O_3, GeO_2, Bi_2O_3, CuO e PdO. To satisfy the needed quantities in Table 2, the cheapest scenario was applied in each of the oxides (Table 3), taking into consideration the required amounts for each oxide in order to produce anode mean samples of 100g.

Table 3 – Oxides cheapest prices from Sigma-Aldrich

Oxide	**Amounts to order**		**Prices**
$PbO.Sb_2O_3$	100g of PbO	100g of Sb_2O_3	28.5€+30.9€
$Pb_{11}Ge_3O_{17}$	100g of PbO	25g of GeO_2	28.5€+205.5€
Pb_3GeO_5	100g of PbO	25g of GeO_2	28.5€+205.5€
$Pb_5Ge_3O_{11}$	100g of PbO	50g of GeO_2	28.5€+520.0€
Bi_2CuO_4	100g of Bi_2O_3	2x25g of CuO	44.8€+42.2€
Bi_2PdO_4	100g of Bi_2O_3	50g of PdO	44.8€+4810€
$Bi_{12}GeO_{20}$	100g of Bi_2O_3	10g of GeO_2	44.8€+109€

The prices shown in Table 3 were chosen in order to obtain the cheapest solution for the intended quantities. It is easy to notice the price discrepancies between the oxides. Oxides like GeO_2, CuO and PdO are much more expensive when compared to the remaining ones, turning their respective compounds into the most costly.

Analyzing the prices, it becomes clear that the cheapest compound to synthesize is ($PbO.Sb_2O_3$). Consulting once more the prices in the very same source, this time for the particular case of this substance, the best option for both of the oxides is 100g of PbO (with purity level above 99.9%) for 27.5€ and 100g of Sb_2O_3 for 29.4€ (with a 5 micrometer granulometry and a purity level of 99%), providing a total cost of 56.9€.

Chapter 3 – A study of Lead and Antimony oxides binary system

From the previous section the lead antimony system with Sb:Pb in a 2:1 ratio was shown to be a possible anode contender, and which was also was relatively inexpensive. A recent study [21] from the universities of Pennsylvania and Philadelphia tested the polarization behavior of several metal alloy binary systems, In-Sb, Sn-Sb, Sb-Bi, and Sb-Pb (with molar percentages of 50%) in the absence of a carbonaceous reductant to demonstrate limits of anode stability. The V-i polarization curves (at an operation temperature of 973K) for the Pb:Sb anode of 1:1 ratio, measured in a closed cell is shown in Figure 15.

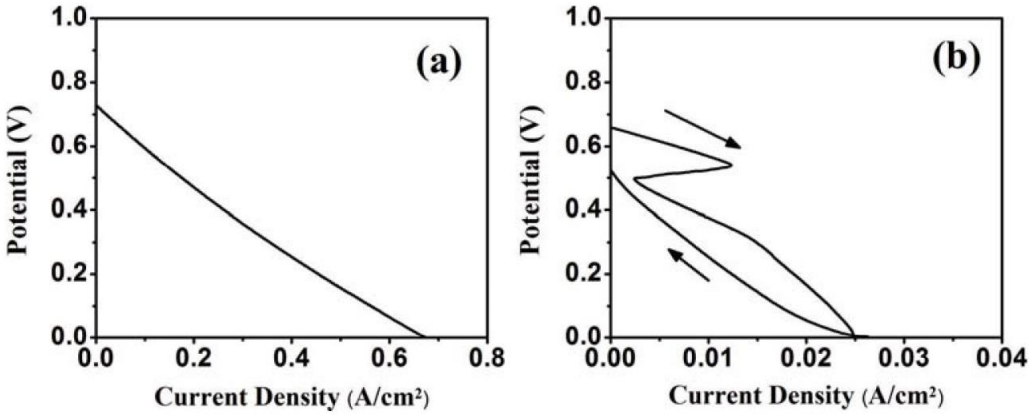

Figure 15 – V-i polarization curves of Pb-Sb alloy of 1:1 ratio (a) initial cell behavior; and (b) repeated experiment after passing a current of 0.25 Acm^{-2} for 18 hours [21]

3.1 Discussion on a literature article that studied the alloy Pb:Sb in a 1:1 ratio

In the matter of the Pb-Sb alloy system studied in this article, it shows quite promising results related to the initial time (Figure 15 (a)). However, the amount of current that can be drawn is shown to be severely limited after longer time operation (Figure 15 (b)). This degradation is demonstrated clearly by (Figure 16) which shows a severe drop in available potential after passing a current of 0.25 Acm^{-2} for times up to 18h. This behavior is accordant with the gradual decreasing oxygen flux across the electrolyte that can be explained by the segregation shown in a photograph of the cross-section cell (Figure 17) after passing enough current to oxidize 120% of the Antimony on the assumption that the lead is unoxidized.

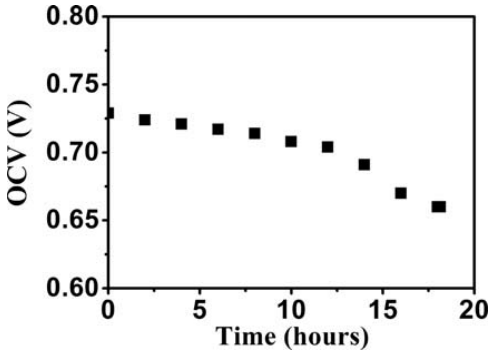

Figure 16 – Pb-Sb alloy system open circuit voltage as function of time while drawing 0.25 A/cm^2 at 973 K. [21]

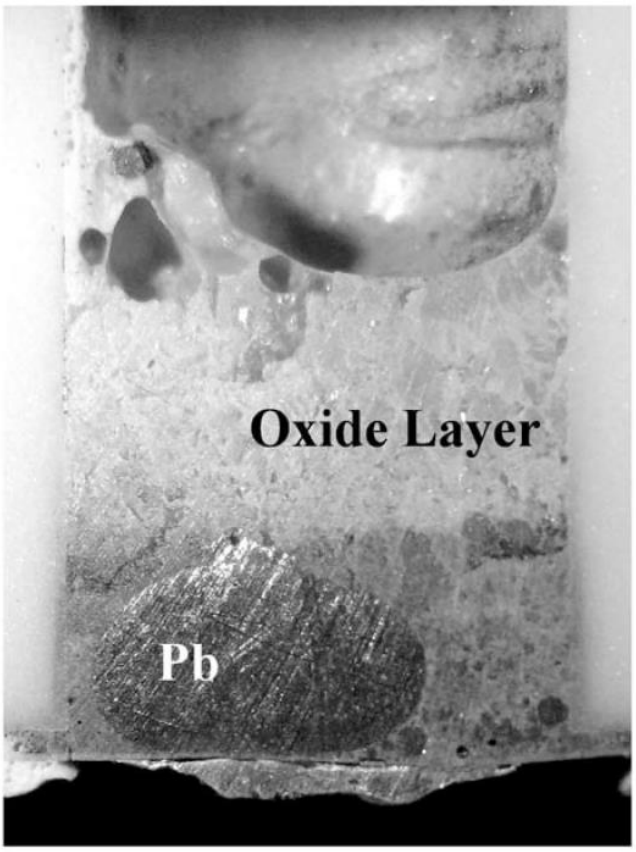

Figure 17 – 50%Pb-50%Sb metal cell cross section, after passing enough charge to oxidize 120% of antimony [21]

3.1.1 Stability difference between the oxides

Consulting the Ellingham diagram (Figure 18) it is clear that the antimony and lead oxidation reactions are located at Gibbs free energies that are less negative than that of carbon oxidation at the temperature of interest providing a lower affinity for oxygen in comparison with that of carbon.

In the direction of increasing negative Gibbs free energy, the first three purple line are related to the lead oxidation reactions respectively PbO_2-Pb_3O_4 and PbO and the fourth purple line represents the antimony oxidation from Sb to Sb_2O_3. The temperature range over which data is available for each line is shown in purple and the thinner green lines are obtained by extrapolation. There are further oxidation states related to the antimony element (Sb_2O_4 and Sb_2O_5), but the current Ellingham diagram shown does not provide this information.

The Ellingham diagram suggests that the antimony oxidation reaction may preferentially occur first due to the fact that it has a significantly higher oxygen affinity than that of lead.

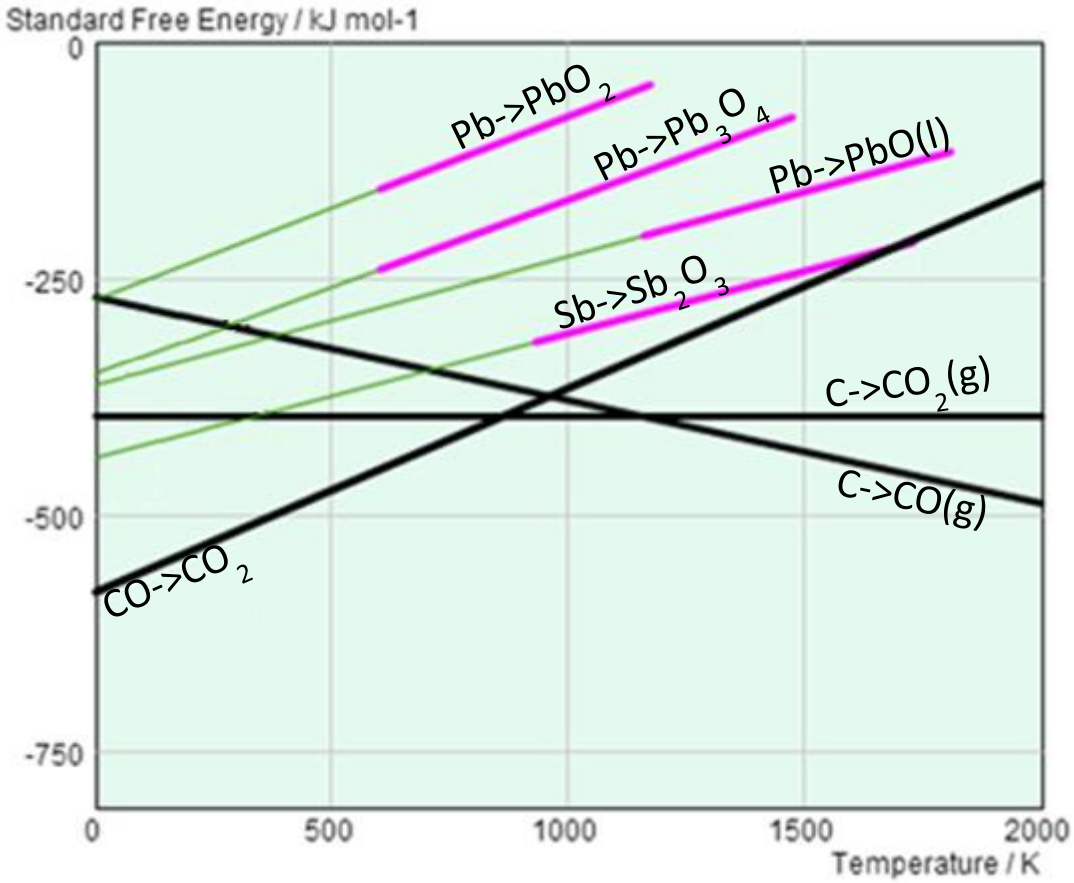

Figure 18 – Carbon, Lead and Antimony oxidation reactions Ellingham diagram [22]

3.1.2 Passed amount of [O^{-2}] during 18 hours with a current density of 0.25 ($A.cm^{-2}$)

Faraday's law of electrolysis relates the "m" mass of the substance liberated at an electrode (in grams) with the "Q" as the total electric charge passed through the substance usually in Coulomb, "F" as Faraday constant (which is 96485.3399 $C.mol^{-1}$), "M" as the molar mass of the substance, and with "z", the number of valence electrons transferred per ion, which in this case is 2 (equation 4).

$$\mathrm{m} = \left(\frac{\mathrm{Q}}{F}\right).\left(\frac{M}{z}\right) \tag{4}$$

By the definition of molar mass, the quotient between "m" and "M" can be written as the number of moles "n" (equation 5). For a simple case of a constant-current electrolysis the same total electric charge "Q" can be expressed as a constant current in one second, therefore "Q" can be replaced by "$I.t$" (equation 6). Using both equation 5 and 6 into the equation 4 it is obtained this way a valid relation, allowing the calculation of the oxygen moles number for a determined period of time (equation 7).

$$\mathrm{M} = \frac{\mathrm{m}}{n} \tag{5}$$

$$\mathrm{Q} = \mathrm{I}.t \tag{6}$$

$$\mathrm{n} = \frac{\mathrm{I.t}}{F.z} \quad (7)$$

Where "I" is the current in Amperes and "t" is the time in seconds

In the previously mentioned scientific paper, a current density is drawn of 0.25 ($A.cm^{-2}$) during 18 hours using an electrolyte porous layer of diameter 0.67 (cm). This diameter implies an area of 0.35 (cm^2), and once the current density drawn was 0.25 ($A.cm^{-2}$) this means the current used was 0.088 (A) (see Calculation 1 below).

$$\text{Current density}(\text{A}.cm^{-2}) = \frac{\text{Current(A)}}{Area(cm^2)} <=> 0.25 = \frac{\mathrm{I}}{3.14\left(\frac{0.67}{2}\right)^2} <=> \mathrm{I} = 0.088\ (\mathrm{A})$$

Calculation 1

Now, from the (7 it is possible to calculate the amount of oxygen ions that passed through the electrolyte within the 18 hours period of the experiment (which corresponds to $18 \times 3600 = 64800\ seconds$), giving the result of 0.0296 moles (Calculation 2).

$$\mathrm{n} = [O^{-2}]_{18h} = \frac{0.088 \times 64800}{2 \times 96485.3399} <=>$$

$$<=> [O^{-2}]_{18h} = 0.0296\ (moles\ of\ [O^{-2}]\ in\ 18\ hours)$$

Calculation 2

In this experiment relative to the 50-mol% alloy, 2 grams of antimony metal was added to the anode. Since the atomic weight of antimony is$121.76(g.mol^{-1})$, from (5, this means the 2 grams of Antimony are equivalent to $0.016 moles$ (Calculation 3).

$$\mathrm{n}_{Sb} = \frac{2}{121.76} = 0.016(moles\ of\ Sb)$$

Calculation 3

The oxidation of antimony metal would form the oxide (Sb_2O_3) giving a ratio of 1 antimony atom for each 1.5 atoms of oxygen. Thus, the expected value of the oxygen moles versus the antimony content would be a ratio close to 1.5. However, dividing the number of moles of [O^{2-}] passed in 18 hours (from Calculation 2) by the number of antimony moles present (in Calculation 3), suggests a value of 1.80, a factor 20% greater than that necessary to oxidize all antimony to Sb_2O_3 (Calculation 4).

$$\mathrm{O}_{ratio} = \frac{[O^{-2}]_{18h}}{\mathrm{n}_{Sb}} <=> \mathrm{O}_{ratio} = \frac{0.0296}{0.016} = 1.802$$

Calculation 4

The anode material, after passing a current of 0.25Acm^{-2} for 18 hours, was sectioned and analyzed under the microscope (Figure 17). The image shows the presence of a ball of unoxidised lead, surrounded by a darker grey region which was stated to be a lead rich oxide and above this layer a lighter yellow region corresponding to the oxide $Pb2SbO_4$. Thus, it is immediately clear that the discussion of section 3.1.1 can be considered an oversimplification. Despite their differing Gibbs free energies, this alloy anode can be oxidized to form a binary oxide mixture, i.e. $Pb2SbO_4$ rather than just the oxide of the metal component that has the highest oxygen affinity, i.e. Sb_2O_3. The presence of this phase also explains why the cell can offer performance for time periods that exceed that which would correspond to total oxidation of antimony (section 3.1.2). Nonetheless, the performance of this cell was still seen to rapidly deteriorate before all the anode material had been

completely oxidized; as demonstrated by the presence of an unoxidised ball of lead. This observation can be related to the Pb rich oxide which surrounds the metallic ball at the bottom of the image, which has previously been reported to offer very low solubility of oxygen and, thus, blocks further oxidation at the anode/electrolyte interface.[21] This effect can be explained with reference to the respective phase diagrams of the Pb-Sb metals and oxides, and is discussed in the following section.

3.2 Possible reasons to explain the oxygen lower ratio and segregation event

3.2.1 Ratio between the metals

Looking to the respective pure metals diagram (Figure 19), for any Pb-Sb ratio there is always liquid phase for both metals at any temperature higher than 650ºC. This suggests the operation temperature of 700ºC (973K), will be sufficient to keep both metals in liquid state when they are not oxidized, regardless their proportion.

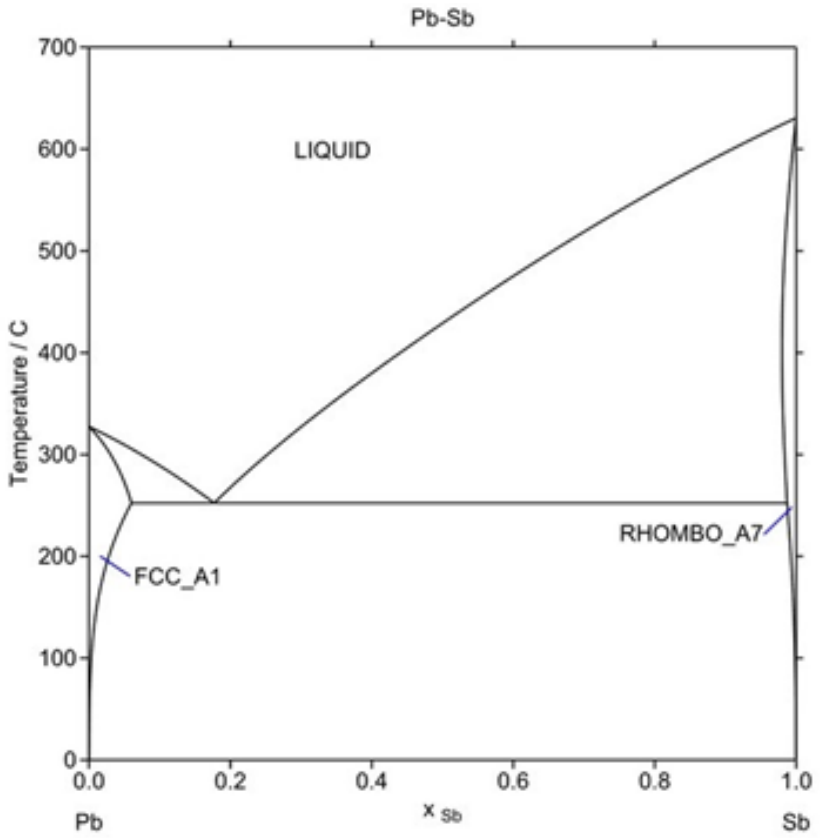

Figure 19 – Pb-Sb phase diagram [23]

In the particular case of the PbO-Sb_2O_3 oxide system phase diagram (Figure 20), 50% ratio of each metal implies the oxides respective percentages of 33% of Sb_2O_3 and 66% of PbO. In these conditions, the melting point temperature is indeed lower than 900ºC. However, on cooling this alloy melt, one will enter into the two phase PbO + $PbSb_2O_4$ region. Moreover, any slight compositional drift from this composition, for example by Sb_2O_3 volatilization (see chapter 4), may take the anode into the two phase PbO + liquid region. The presence of $PbSb_2O_4$ in the microscopy image of Figure 17, therefore, can be explained due to cooling the molten anode into the two phase PbO + $PbSb_2O_4$ region. On the contrary, the presence of PbO in the microscopy image can be explained by either cooling or compositional drift, or both.

The latter of these, the presence of compositional drift, could explain the degradation of the open circuit voltage noted along the 18 hours upon operation. The solid β phase of PbO could deposit at the anode/electrolyte interface blocking further electrochemical operation. This conjecture is coherent with the described results of the Figure 17 in the article [21], because their analysis revealed that the gray material surrounding metallic Pb article was an oxide rich in Pb. It should be noted that a better choice of metallic composition would have been Pb:2Sb corresponding to the oxide phase $PbSb_2O_4$ as this oxide would melt congruently, thus, not segregate into two phases on cooling, and would also be a safer composition to choose that would provide a liquid phase of composition much further from the PbO + liquid phase region. For these reasons it was the intended composition to be studied in the current work.

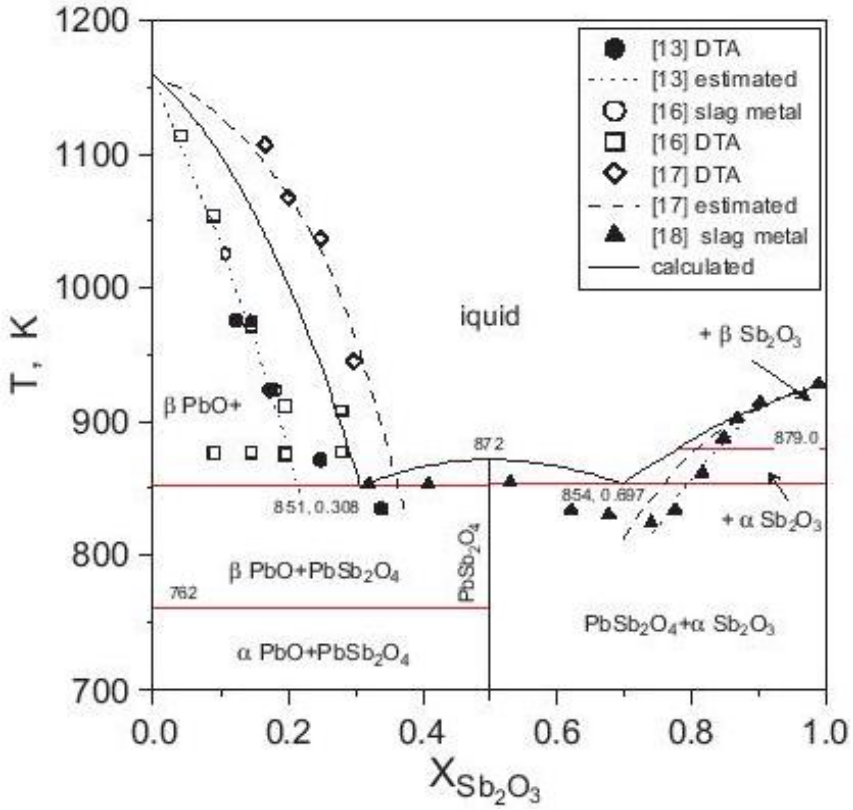

Figure 20 – $PbO\text{-}Sb_2O_3$ Phase diagram [26]

3.2.2 The pertinent oxidation state

It is also important to highlight that enough current was applied to oxidize 120% of antimony, upon assuming no lead oxidation. Therefore, the pertinent oxidation state in this situation could potentially be superior to the Sb^{3+} state (corresponding to Sb_2O_3), for example Sb^{4+} (in Sb_2O_4) or Sb^{5+} (from Sb_2O_5). If so, it is relevant to examine the respective phase diagrams these higher oxidation states of Sb (Figure 21 and Figure 22). Both diagrams show that the operation temperature of 973K is not enough to keep the system in the liquid phase according to the 50% molar proportions of the literature study.

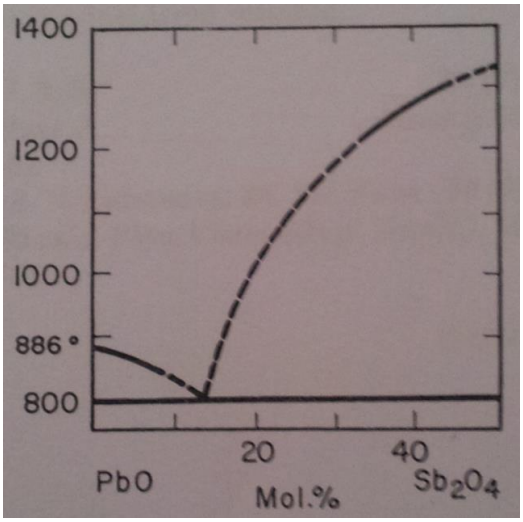

Figure 21 – PbO-Sb_2O_4 Phase diagram [24]

Thus, the impaired performance could as well be occurring due to the “over” oxidation of Sb. However, as it was mentioned before, there is no information about these oxidation levels in available Ellingham diagrams and this lack of information limits this discussion. However, following the microscopy image of the aforementioned article the presence of PbO appears to be the most plausible reason for the depleted performance.

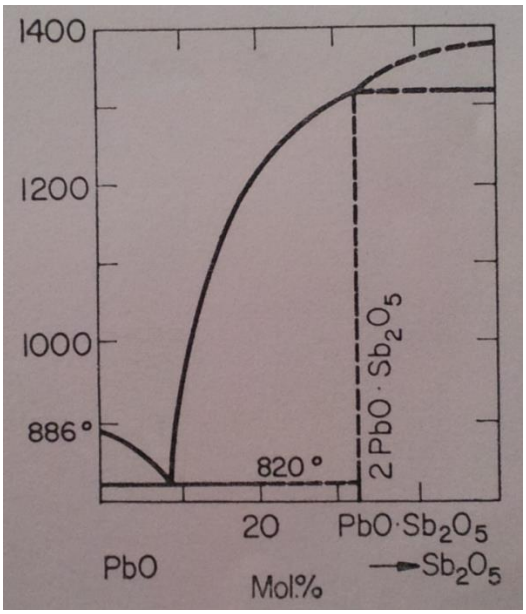

Figure 22 – PbO-Sb_2O_5 Phase diagram [24]

3.2.3 Other factors

The densities of each of the oxides are very dissimilar. The lead oxide density (9.53 $g.cm^{-3}$) is almost twice of the density of the antimony oxide (5.2 $g.cm^{-3}$ in α-form and 5.67 $g.cm^{-3}$ in β-form). This density difference might as well be contributing to lower the homogeneity of the anode with lead rich oxide phase being that found at the bottom layer corresponding to the anode/electrolyte

interface while leaving the upper layer more antimony rich and closer to the $PbSb_2O_4$ composition which would form on cooling. This factor could also explain the micrograph shown in Figure 17.

Chapter 4 – Theoretical vapor pressure analyses of components within the Pb-Sb system

4.1 Introduction

In the previous chapter of this work were discussed possible reasons to explain the lead segregation event in the previously mentioned work [21]. As briefly mentioned one possible reason to justify this event would be the existence of elemental loss due to volatilization. Thus, this chapter is dedicated to calculating the respective vapor pressures of the expected Sb-Pb materials. The temperature dependence of vapor pressure values of the pure substances were easily obtained using the Factsage software database [23]. On the other hand, the vapor pressure values of the reduced alloys as well as binary oxides were calculated separately using constant temperature values (found in literature) to provide the concentration dependence of vapor pressure within the binary mixtures.

4.2 Theoretical principles, assumptions and expressions used in the calculations

In this section some thermodynamic expressions necessary to understand this chapter will be defined before the revelation of the calculated results. Some assumptions were necessary to perform the calculations. The first assumption is that of the equilibrium state in all vaporization reactions. This is valid because, in the analyzed source [21], the cell was operated at constant pressure and temperature.

The Gibbs free energy of a vaporization reaction can be expressed as:

$$\Delta \mathrm{G} = G_v - G_l \tag{8}$$

Where "$\Delta \mathrm{G}$" is the Gibbs free energy of the vaporization reaction, "G_v" is the Gibbs free energy of the vapor phase and "G_l" is the Gibbs free energy of the liquid phase

The Gibbs free energy is defined as a function of the enthalpy "H", temperature "T" and Entropy "S" such as:

$$\mathrm{G} = \mathrm{H} - T.S \tag{9}$$

Using the definition of free energy (equation 9) in the equation 8 it is possible to obtain an expression of the Gibbs energy variation for the vaporization reaction (equation 10), as:

$$\Delta \mathrm{G} = (H_v - T.S_v) - (H_l - T.S_l)$$

$$\Delta \mathrm{G} = (H_v - H_l) - T.(S_v - S_l)$$

$$\Delta \mathrm{G} = \Delta \mathrm{H} - T.\Delta \mathrm{S} \tag{10}$$

It is possible to relate the equilibrium constant with the standard Gibbs free energy (equation 11). In this relation "R" is the universal gas constant (which is 8,314 $\mathrm{J.K^{-1}.mol^{-1}}$), "$\mathrm{T}$" is the temperature (in Kelvin) and "K_{eq}" the equilibrium constant of this vaporization reaction.

$$\Delta \mathrm{G} = -R.\mathrm{T}.\ln(K_{eq}) \tag{11}$$

The equilibrium constant of the vaporization reaction "K_{eq}" is often called "vapor pressure" "V_p", and it is literally the partial pressure "$P_{partial}$" of the compound in the gas. Replacing the

equilibrium constant by the vapor pressure and using the equation 10 in the equation 11 it is obtained the relation later used as a linear chart representation in the results analysis equation 12.

$$\Delta \mathrm{H} - T.\Delta S = -R.\mathrm{T}.\ln(Vp)$$

$$\ln(Vp) = \frac{\Delta \mathrm{H} - T.\Delta S}{-R.\mathrm{T}} = \frac{\Delta \mathrm{H}}{-R.\mathrm{T}} + \frac{-T.\Delta S}{-R.\mathrm{T}} = \frac{\Delta \mathrm{H}}{-R.\mathrm{T}} + \frac{\Delta S}{R}$$

$$\ln(Vp) = \frac{\Delta \mathrm{H}}{-R}.\left(\frac{1}{T}\right) + \frac{\Delta S}{R} \tag{12}$$

Through the logarithm rules equation 13, it is possible to convert any logarithm of something "A" with certain base number "b_1" into another logarithm of a different base number "b_2".

$$\log_{b_1}(A) = \frac{\log_{b_2}(A)}{\log_{b_2}(b_1)} \tag{13}$$

So, in this specific case, the conversion from Neperian logarithm to the base ten logarithm would be:

$$\ln(Vp) = \log_e(V_p) = \frac{\log_{10}(V_p)}{\log_{10}(e)} \tag{14}$$

Applying this equation 14 into the equation 12, the linear relation used for the pure substances in this chapter was found (equation 15):

$$\ln(Vp) = \frac{\log_{10}(V_p)}{\log_{10}(e)} = \frac{\Delta \mathrm{H}}{-R}.\left(\frac{1}{T}\right) + \frac{\Delta S}{R}$$

$$\log_{10}(Vp) = \log_{10}(e).\left[\frac{\Delta \mathrm{H}}{-R}.\left(\frac{1}{T}\right) + \frac{\Delta S}{R}\right]$$

$$\log_{10}(Vp) = \frac{\Delta \mathrm{H}.\log_{10}(e)}{-R}.\left(\frac{1}{T}\right) + \frac{\Delta S.\log_{10}(e)}{R} \tag{15}$$

In order to achieve a linear representation, the chosen "x" and "y" variables will provide the used axis in the subsequent plots. Analogously with the mathematical equation of a straight line ($\mathrm{y} = m.x + b$) the "y" axis will contain the values of "$\log_{10}(V_p)$" and the "x" axis will contain an inverse of the temperature "$1000/T$" (the multiplication of this term with a factor of 1000 is in order to ease the observation of the differences in the numbers along the scale). The slope "m" will be given by the " $\frac{\Delta \mathrm{H}.\log_{10}(e)}{-R}$ " term, the same way as the intercept will be the " $\frac{\Delta S.\log_{10}(e)}{R}$ " part.

In pure systems, the vapor pressure of the substances was plotted according to equation 15, although, in the mixture analysis a further approximation was necessary. In a gas mixture at low pressure (1 atm), the activity is approximately equal to the ratio of the partial pressure of the gas over the vapor pressure of itself within a pure solution (equation 16). Since the partial pressure corresponds to the "vapor pressure", then, the vapor pressure of a compound within a mixture will be equal to the multiplication of the correspondent activity value to that mixture with the vapor pressure of that compound within itself (equation 17).

$$a_i = \frac{P_{mix}}{P_{pure}} = \frac{Vp_{mix}}{Vp_{pure}} \quad (16)$$

$$Vp_{mix} = a_i . Vp_{pure} \quad (17)$$

Where the "P_{mix}", "P_{pure}", "Vp_{mix}", the "Vp_{pure}" and the "a_i" stand for the partial pressures and vapor pressures of the compound within the mixture and within itself and the activity of the "i" compound respectively

A new relation was then used to analyze the vapor pressures of each compound within a mixture by simply introducing this new partial pressure inside the logarithm of equation 15 in order to replace the vapor pressure of a pure substance to the one within a mixture (equation 18).

$$\log_{10}(Vp_{mix}) = \frac{\Delta H.\log_{10}(e)}{-R}.\left(\frac{1}{T}\right) + \frac{\Delta S.\log_{10}(e)}{R}$$

$$\log_{10}(a_i . Vp_{pure}) = \frac{\Delta H.\log_{10}(e)}{-R}.\left(\frac{1}{T}\right) + \frac{\Delta S.\log_{10}(e)}{R} \quad (18)$$

4.3 Vapour pressure of substances

4.3.1 Vapour pressures of pure substances along with temperature

As a first approach, the vapor pressures of the substances within themselves were plotted as a function of the temperature (Figure 23). The graph shows that the vapor pressures related to the antimony oxide phase changes are much higher than the other substances.

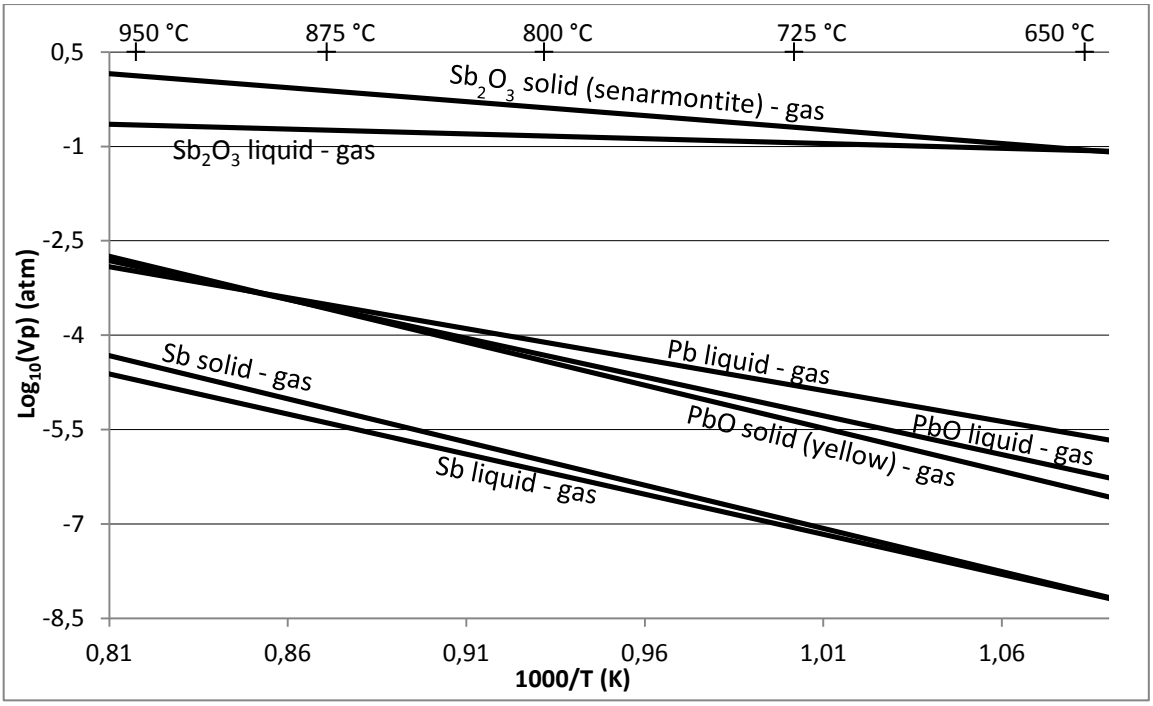

Figure 23 – Vapor pressure (Log_{10}[Vp (in atm)]) of all substances within themselves along with temperature (1000/[T(in K)]) (data collected from Factsage software)[23])

In the matter of stability, the reduced antimony metal phase changes have the lowest vapor pressures. This highlights the interesting result that antimony is the most stable metal of all materials in its reduced form but the least stable in its oxidized form. Vapor pressure values differences between solid structures of Sb_2O_3 (isometric senarmontite and orthorhombic valentinite) as well as red or yellow PbO powder (with tetragonal or orthorhombic structures respectively) were considered, but the observed differences of each of these phases are shown to not be relevant when compared to the overall order of magnitude differences noted between the antimony and lead compounds.

The lead solid-gas vapor pressure values along with the temperature were also observed, but those proved to be pretty much coincident (at this order of magnitude) with the ones of lead solid-liquid vapor pressure. Moreover, since at those temperatures the reduced lead is beyond its melting point, all of it will be in liquid phase, decreasing drastically the relevance of this information in the plot.

4.3.2 Vapour pressures of substances within a mixture

In the matter of oxide and reduced metals behavior within binary mixtures, it was not possible to plot such a consistent vapor pressure variation along with the temperature due to insufficient data from the literature sources. However, at constant temperatures, the activity values found in some sources[26],[27] were useful to the aim of this study. The data obtained from the literature only allow a brief analysis from the vapor pressure values of an oxide within a mixture (formed by both lead and antimony oxides), and analogously the same for reduced metals within a mixture (in this case, formed by both lead and antimony reduced metals). Since a temperature variation was not possible to achieve consistently, the vapor pressure values were plotted along with the antimony proportion increase from 0 to 1.

4.3.2.1 Oxides vapour pressures within an oxides mixture

The oxides activity values series found at the constant temperatures of 850, 750 and 700 °C [26] (along with the antimony trioxide ratio) allowed a simple conversion to the respective vapor pressure values (at those temperatures). The vapor pressure values within a mixture were then obtained through simply multiplying those activity values with the vapor pressure values of the substances within themselves at those temperatures. For three distinct temperatures, both oxides vapor pressures were plotted (Figure 24 and Figure 25), thus obtaining six series of vapor pressure values.

The antimony trioxide vapor pressure values within the oxides mixture in Figure 24 are always superior for any of those temperature values in comparison with the lead oxide ones in Figure 25, and this is observed to also be valid for all compositional ratios. As expected, the vapor pressure of an oxide increases along with its own ratio, and these values, were once more displayed in a logarithmic form, enabling this way, the observation of both ascendant and descendent tendencies along with the increase of antimony trioxide ratios.

Since the calculated vapor pressure values for the three distinct temperatures are within our cell range operation temperatures, a tendency between the three temperatures was plotted for gap ratios of 0.2 in attempt to predict how the vapor pressure would behave along with the temperature. Much higher Sb_2O_3 vapor pressures can be observed than those of PbO and, as expected, the Sb_2O_3 vapor pressure increases with increasing Sb content.

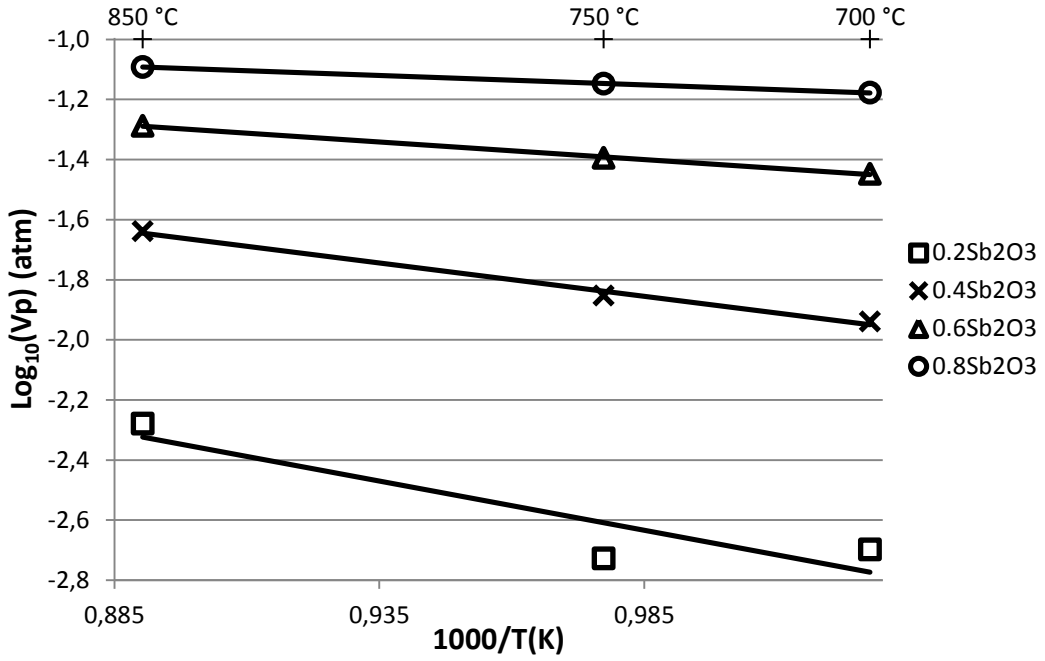

Figure 24 – Sb_2O_3 vapor pressure (in atm) base ten logarithm along with the temperature for distinct Sb_2O_3 ratios (data used from Factsage software [23],[26])

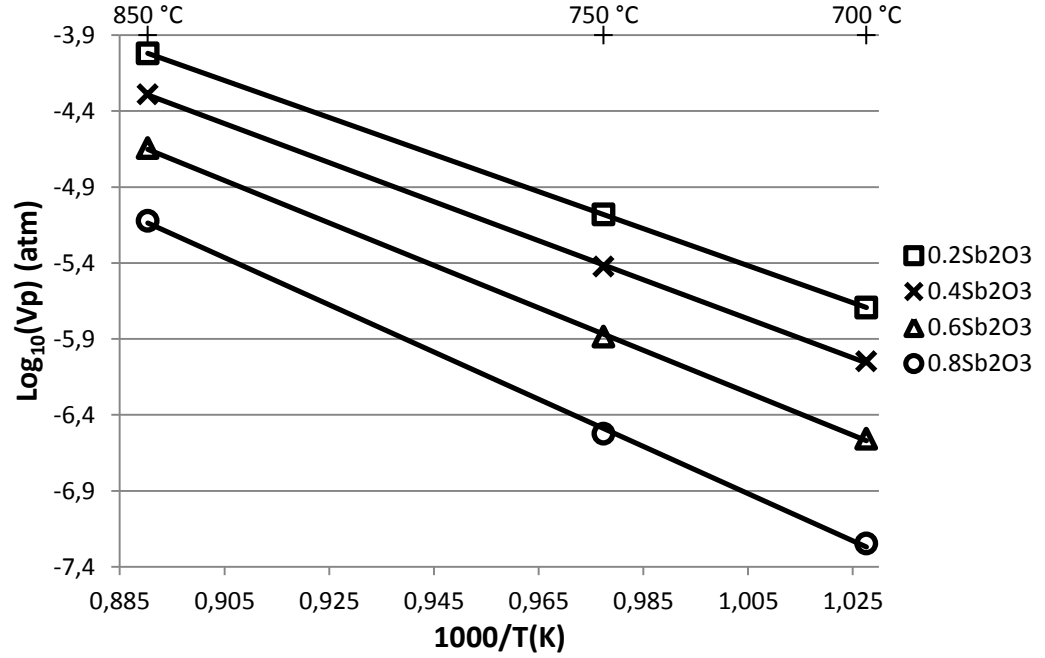

Figure 25 – PbO vapor pressure (in atm) base ten logarithm along with the temperature for distinct Sb_2O_3 ratios (data used from Factsage software [23],[26])

4.3.2.2 Reduced metals vapour pressures within a mixture

Just like in the oxides section, the series of vapor pressure values were calculated by the simple multiplication of the activity values with the vapor pressure values of the substances within themselves at the same temperature. Unfortunately, the only source of data [27] found for this task contained only calculated and experimental series of activity values for a specific constant temperature of 923 K. The experimental values were used to try to achieve a vapor pressure variation along with the temperature, but no tendency line between different temperatures data could be obtained. Therefore constant values of activity were considered along with the increase of temperature in each specific ratio of oxides. This approximation is considered realistic because in gaseous form, intermolecular interactions can be neglected due to larger distance between particles (producing this way almost no influence in the effective concentration levels), and in a liquid phase, the mean strength of interactions is considered to be constant between every particle and its surrounding vicinity (assuming this way that the molecular forces in the three possible bonds of this system are approximately equal). Due to this assumption, the series of values in each ratio were then obtained through simple multiplication of the vapor pressure values of the pure metals with the activity values of those metals for each ratio (Figure 26 and Figure 27).

In the matter of reduced metals ratios between both metals, the lead now shows the higher values of vapor pressure, which is in accordance with the values of the pure substances observed in Figure 23. In both graphics, as expected, for a certain constant temperature the vapor pressure of certain element decreases along with its decreasing percentage within the mixture, as that is also true for the activity values (used in its calculation).

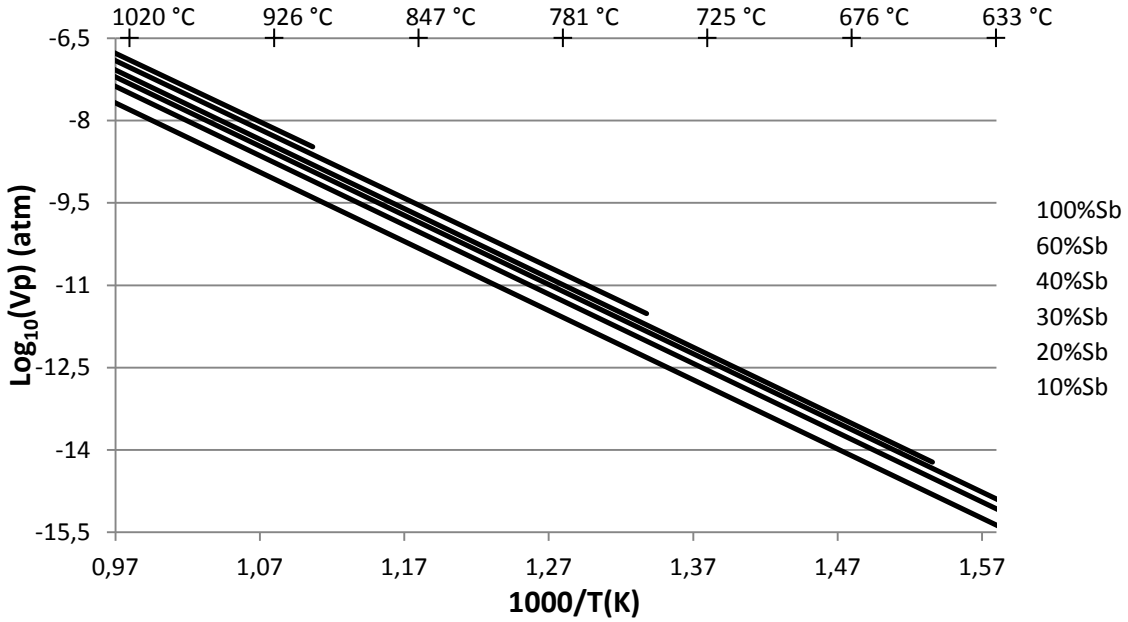

Figure 26 – Sb vapor pressure (in atm) base ten logarithm along with the temperature for distinct Sb ratios (data used from Factsage software [23],[26])

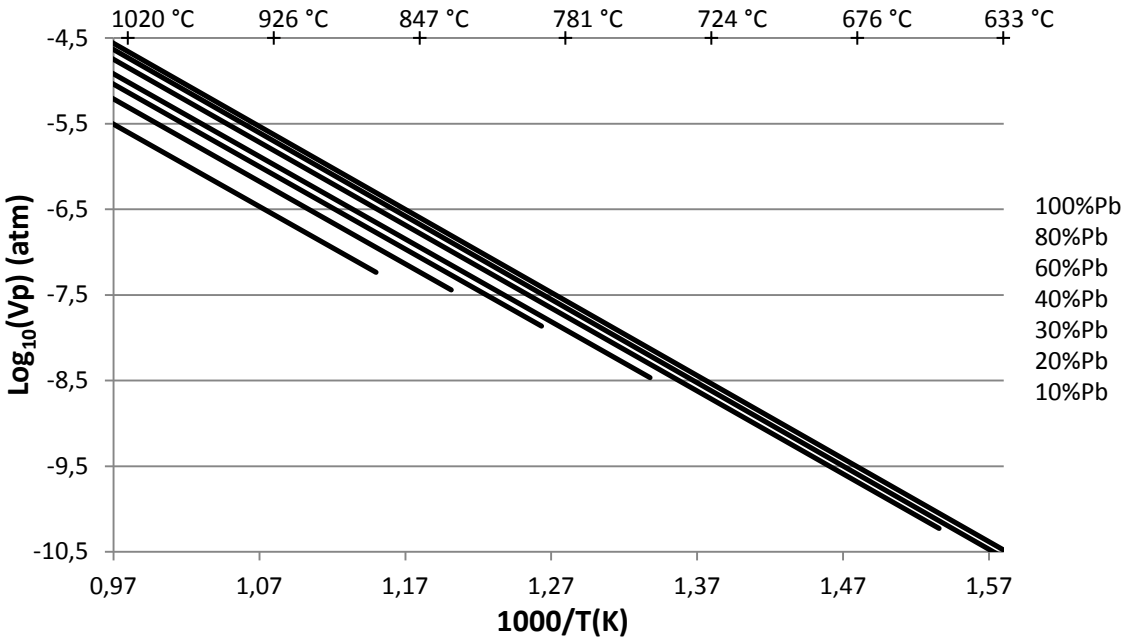

Figure 27 – Pb vapor pressure (in atm) base ten logarithm along with the temperature for distinct Sb ratios (data used from Factsage software [23],[26])

The constant activity values approximation with temperature was only applied for gaseous or liquid forms (due to constant or no influence at all in the activity levels, respectively as previously discussed). This is the reason why the length of the lines differs for each proportion. The lowest value of temperature that allows the liquid phase existence (which means significant vapor pressure data from this point forward), which is the melting point, is different in each mixture. Some mixtures were discarded because the lines would not add any further information to the chart tendencies or it would hamper the reading and interpretation of it. The linear trend lines displayed in all charts were faithful to the calculated point disposition, and due to the existence of almost no standard deviations, they served well its purpose to summarize the behavior instead of individual point symbols.

4.4 Conclusion of the vapour pressure analysis

As seen in the previous oxides and pure metals vapor pressure studies, the antimony oxide can be predicted to demonstrate a very unstable behavior at the operation temperature conditions with a huge tendency for volatilization. Due to this fact, one can imagine that initially the cell would operate starting from the reduced metals, promoting their oxidation by pumping oxygen ions from the cathode through the electrolyte to the anode. However, as soon as the anode is oxidized the antimony oxide is likely to volatilize, leading to compositional drift and potential cell degradation by entering into the PbO + liquid phase region (Figure 20), as suggested in the previous chapter,

In the presence of a carbonaceous reductant (such as plastic) the electrochemical oxidation of the liquid anode will be reversed by oxidation of the fuel, the anode in turn itself being instantaneously reduced. However, under high load, high fuel utilization, gas leaks, or fuel supply interruption it is possible that oxidation of the liquid anode may occur, which could result in subsequent Sb_2O_3 volatilization and compositional drift of the anode. In the literature study of Pb:Sb in a 1:1 ratio [21] the experiments were performed by firstly flowing H_2, then replacing this atmosphere with He and finally closing the electrochemical cell. The aim of this study was to test the stability of the molten anodes upon operation without the presence of a reductant. However, from the Ellingham diagram of the Sb-system (Figure 18), one can predict that Sb will have likely

been oxidized in the He atmosphere used, even without electrochemical oxidation being performed, Thus, to avoid similar difficulties in the current project, a closed cell container model was carefully considered in the next chapter where the anodic compartment is of small volume and sealed directly in the reducing environment. By this way one aims to properly analyze the alloy system viability limiting antimony evaporation and compositional drift.

Chapter 5 - Experiments

5.1 Volatilization quantification

5.1.1 Number of moles in the liquid metal volume

The present section of this work explains the calculation procedures to determine potential molar losses due to Sb_2O_3 volatilization within each of the metal compositions of Pb:Sb and Pb:2Sb. As previously outlined, according to the PbO-Sb_2O_3 binary oxide phase diagram, it is expected that the PbO.Sb_2O_3 composition melts congruently. This composition corresponds to a pure metal proportion of 33%Pb and 66%Sb, once there are two antimony atoms for each lead atom (Pb:2Sb). In contrast the proportion studied by the previously mentioned work [21] is a 50% pure metal proportion of each of the Pb and Sb components (Pb:Sb). In this section, the calculation of both proportions will be presented.

According to the definitions of molar mass "m_{molar}" and molar volume "V_{molar}", shown respectively in the equation 5 and 19, it can be demonstrated that the density (equation 20) can be calculated through the molar mass and molar volume.

$$V_{\mathrm{molar}} = \frac{\mathrm{V}}{n} \tag{19}$$

Where "V_{molar}" is the molar volume, "V" the geometric volume and "n" is the number of moles

$$\rho = \frac{\mathrm{m}}{V} \tag{20}$$

Where "ρ" is the density, "m" the mass and "V" is the volume

By applying the **Error! Reference source not found.** and equation 19 in the equation 20, it is easy to demonstrate that the quotient between mass and volume is also valid using molar mass and molar volume (equation 21), thus validating this respective equation to calculate the molar volumes of antimony and lead.

$$\rho = \frac{m_{\mathrm{molar}}}{V_{\mathrm{molar}}} \tag{21}$$

The metals density changes along with temperature. In this work, the density variation for lead and antimony densities with the temperature is defined in equations 22 [28] and 23 [28].

$$\rho_{(Pb)} = 11{,}560 - 16{,}5 \times 10^{-4}.T + 1{,}85 \times 10^{-7}T^{-2} \tag{22}$$ **[28]**

Where "$\rho_{(Pb)}$" is the lead density in $10^3 \times Kg.m^{-3}$ and "T" is the temperature in K

$$\rho_{(Sb)} = 6{,}953 - 4{,}65 \times 10^{-4}T - 0{,}964 \times 10^{-7}T^{-2} \tag{23}$$ **[28]**

Where "$\rho_{(Sb)}$" is the antimony density in $10^3 \times Kg.m^{-3}$ and "T" is, once more, the temperature in K

Since the cell operation temperature is 973K, this condition was applied in equations 22 and 23 in order to determine the respective densities for each one of the two metals at this temperature ($\rho_{(Pb)} = 9{,}95 \times 10^3 (Kg.m^{-3})$; $\rho_{(Sb)} = 6{,}50 \times 10^3 (Kg.m^{-3})$). Afterwards, using equation 21, and introducing the relative molar mass values of each pure metal ($m_{\mathrm{molar}_{(Pb)}} = 207{,}21 \times 10^{-3}\ Kg.mol^{-1}$ and $m_{\mathrm{molar}_{(Sb)}} = 121{,}76 \times 10^{-3}\ Kg.mol^{-1}$), the respective molar volumes were then calculated ($V_{\mathrm{molar}_{(Pb)}} = 2{,}08 \times 10^{-5}\ m^3.mol^{-1}$; $V_{\mathrm{molar}_{(Sb)}} = 1{,}87 \times 10^{-5}\ m^3.mol^{-1}$).

The total molar volume will be formed by the sum of both components, each one in its own percentage (equation 24). Since two different ratios were analyzed, both calculations were presented each with its own ratio, where x is the fraction of antimony (Calculation 5.1 and Calculation 5.2).

$$V_{molar} = (1 - x).V_{\text{molar}_{(Pb)}} + x.V_{\text{molar}_{(Sb)}} \quad (24)$$

[Pb:Sb] -> $V_{molar_{[\text{Pb:Sb}]}} = 0{,}5.V_{\text{molar}_{(Pb)}} + 0{,}5.V_{\text{molar}_{(Sb)}}$

$$V_{molar_{[\text{Pb:Sb}]}} = 0{,}5 \times 2{,}08 \times 10^{-5} + 0{,}5 \times 1{,}87 \times 10^{-5}$$

$$V_{molar_{[\text{Pb:Sb}]}} = 1{,}98 \times 10^{-5}(m^3.mol^{-1})$$

Calculation 5.1

[Pb:2Sb] -> $V_{molar_{[\text{Pb:2Sb}]}} = \frac{1}{3}.V_{\text{molar}_{(Pb)}} + \frac{2}{3}.V_{\text{molar}_{(Sb)}}$

$$V_{molar_{[\text{Pb:2Sb}]}} = \frac{1}{3} \times 2{,}08 \times 10^{-5} + \frac{2}{3} \times 1{,}87 \times 10^{-5}$$

$$V_{molar_{[\text{Pb:2Sb}]}} = 1{,}94 \times 10^{-5}(m^3.mol^{-1})$$

Calculation 5.2

The volume of the anodic chamber of the cell can be defined the same way as a cylinder volume (equation 25) and for this section it was considered a height "h" and diameter to be respectively 2 and 1 cm, and this way, the obtained correspondent value for the volume of the anodic chamber was $0{,}785cm^3$. Assuming only half of the total volume is filled with liquid, then the volume of the liquid in the container will be $0{,}393 \times 10^{-6}m^3$.

$$V = h.(\pi.r_{anode}^2) \quad (25)$$

Using once more the equation 19 and knowing both the total geometric and molar volumes, it is possible to calculate the total number of moles contained within the proposed anode volume for both molar ratios (Calculation 6.1 and Calculation 6.2).

[Pb:Sb] -> $n_{[\text{Pb:Sb}]} = \frac{V}{V_{molar_{[\text{Pb:Sb}]}}}$

$$n_{[\text{Pb:Sb}]} = \frac{0{,}393 \times 10^{-6}}{1{,}98 \times 10^{-5}} \cong 0{,}0198\ mol$$

Calculation 6.1

[Pb:2Sb] -> $n_{[\text{Pb:2Sb}]} = \frac{V}{V_{molar_{[\text{Pb:2Sb}]}}}$

$$n_{[\text{Pb:2Sb}]} = \frac{0{,}393 \times 10^{-6}}{1{,}94 \times 10^{-5}} \cong 0{,}0202\ mol$$

Calculation 6.2

In a binary system, a certain percentage of one of the elements directly implies that the other element's quantity is the remaining part up to 100% (equation 26). So, after calculating the total number of moles within the geometrical volume for both alloys, it was obtained a total quantity of moles from each lead and antimony element in those proportions as well, applying equation 26

for each of the metals within both Pb:Sb and Pb:2Sb ratios (Calculation 7.1, Calculation 7.2, Calculation 8.1 and Calculation 8.2) where the "x" ratios of antimony are 0,5 and two thirds respectively.

$$n_{(Sb)} = \mathrm{x}.n \rightarrow n_{(Pb)} = (1 - \mathrm{x}).n \quad (26)$$

Where "$n_{(Pb)}$", "$n_{(Sb)}$" and "n" are respectively the Pb and Sb and total number of moles within and of the mixture calculated called upon the equation 19

$$n_{(Pb)_{[\mathrm{Pb:Sb}]}} = \left(1 - x_{[\mathrm{Pb:Sb}]}\right).n_{[\mathrm{Pb:Sb}]}$$

$$n_{(Pb)_{[\mathrm{Pb:Sb}]}} = (1 - 0{,}5) \times 0{,}0198 \cong 0{,}0099\ mol$$

Calculation 7.1

$$n_{(Sb)_{[\mathrm{Pb:Sb}]}} = x_{[\mathrm{Pb:Sb}]}.n_{[\mathrm{Pb:Sb}]}$$

$$n_{(Sb)_{[\mathrm{Pb:Sb}]}} = 0{,}5 \times 0{,}0198 \cong 0{,}0099\ mol$$

Calculation 7.2

$$n_{(Pb)_{[\mathrm{Pb:2Sb}]}} = \left(1 - x_{[\mathrm{Pb:2Sb}]}\right).n_{[\mathrm{Pb:2Sb}]}$$

$$n_{(Pb)_{[\mathrm{Pb:2Sb}]}} = \left(1 - \frac{2}{3}\right) \times 0{,}0202 \cong 0{,}0067\ mol$$

Calculation 8.1

$$n_{(Sb)_{[\mathrm{Pb:2Sb}]}} = x_{[\mathrm{Pb:2Sb}]}.n_{[\mathrm{Pb:2Sb}]}$$

$$n_{(Sb)_{[\mathrm{Pb:2Sb}]}} = \frac{2}{3} \times 0{,}0202 \cong 0{,}0135\ mol$$

Calculation 8.2

5.1.2 Theoretical Sb_2O_3 number of moles within the gas volume

As shown in Chapter 4, the antimony oxide vapor pressure is much higher than the lead oxide. In order to predict some of the operating conditions of a solid oxide fuel cell with lead and antimony alloy anodes, the potential compositional drift due to Sb_2O_3 volatilization was estimated.

From the data used to produce section 4.3.2.1 of the previous chapter the antimony oxide vapor pressure values were taken in the way that the ratios match the reduced metal proportions of Pb:Sb and Pb:2Sb. Assuming the ideal gas law (equation 27) the conditions were then applied for both different ratios (Calculation 9.1 and Calculation 9.2). Both ratios considered the same conditions of container volume (with 1cm of diameter and 2 cm height, which corresponds to a total anodic chamber volume of 0,393 cm^3), where all of this volume is filled by the molten metal and the other half is that of the gas phase. Temperature was 973 kelvin and R was 82,05736 $cm^3.atm.K^{-1}.mol^{-1}$.

$$\mathrm{P}.\mathrm{V} = n.R.\mathrm{T} \quad 27$$

Where the "P", "V", "n", "R" and the "T" represent the gas pressure (in these cases the vapor pressures of each ratio), gas phase volume (which is half the anode chamber anode volume), number of moles, ideal gas constant and the temperature respectively.

$$n_{(Sb_2O_3 \text{ in [Pb:Sb]})_{lost}} = \frac{Vp_{(Sb_2O_3 \text{ in [Pb:Sb]})} \cdot \mathrm{V}}{R.\mathrm{T}}$$

$$n_{(Sb_2O_3 \text{ in [Pb:Sb]})_{lost}} = \frac{5 \times 10^{-2} \times 0{,}393}{82{,}05736 \times 973{,}15 \times 2} = 1{,}23 \times 10^{-7} mol$$

Calculation 9.1

$$n_{(Sb_2O_3 \text{ in [Pb:2Sb]})_{lost}} = \frac{Vp_{(Sb_2O_3 \text{ in [Pb:2Sb]})} \cdot \mathrm{V}}{R.\mathrm{T}}$$

$$n_{(Sb_2O_3 \text{ in [Pb:2Sb]})_{lost}} = \frac{2{,}33 \times 10^{-2} \times 0{,}393}{82{,}05736 \times 973{,}15 \times 2} = 0{,}58 \times 10^{-7} mol$$

Calculation 9.2

5.1.3 Antimony volatilization conclusion

Now that both gas and liquid molar quantities were determined, it is possible to affirm the molar antimony losses due volatilization in both ratios are very small for this anodic chamber volume when compared to the total number of moles of antimony given in Calculation 7.2 and Calculation 8.2. For this reason, it seems justifiable to create a cell using a closed container of this small volume, preventing further volatilization beyond the theoretical equilibrium point, allowing the anode materials to be tested while preventing significant compositional drift.

5.2 First cell project

The purpose of this cell is to study the electrochemical behavior of the Pb:Sb and Pb:2Sb alloy systems as an anode while preventing compositional drift due to volatilization. Starting from the pure metals in the right proportions for the Pb:Sb ratio inside a closed container, a cell model (Figure 28 - B) was designed so that latter on; the real cell (Figure 28 - A) could be built.

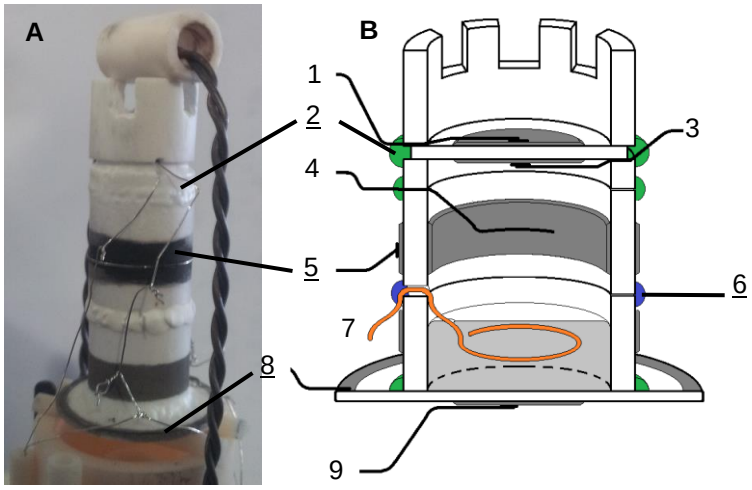

Legend:
1 – Outer electrode of pump, **2** – Low temperature sealing glass, **3** – Inner electrode of pump,
4 – Inner electrode of oxygen sensor, **5** – Outer electrode of oxygen sensor
6 – High temperature sealing glass, **7** – Rhenium wire of working electrode
8 – Reference electrode, **9** – Counter electrode

Figure 28 – The built closed container cell (**A**) and its scheme (**B**) revealing the inner parts

5.2.1 The pump

This cell design contains an oxygen pump (represented in the numbers 1 and 2 in Figure 28) providing the adjustment of the oxygen activity in the gas phase by electrochemical pumping (equation 28).

$$O_2 + 4e^- \rightarrow 2O^{2-} \quad (28)$$

Using the deduced relation (equation 7) from Faraday's law already defined in chapter 3, given a constant current "I" during a certain amount of time, it is possible to calculate the number of moles correspondent to the oxygen ions that passed through the pump.

5.2.2 The sensor

Within this cell there is also a sensor (whose representation belongs to the numbers 3 and 4) that through measuring its voltage between inside and outside it is possible to estimate the oxygen partial pressure inside anodic chamber by applying the Nernst equation (equation 29).

$$E_{red} = E^0_{red} - \frac{R.\mathrm{T}}{n_e.F} ln\left(\frac{\mathrm{p}O_{2_{red}}}{\mathrm{p}O_{2_{ox}}}\right) \quad (29)$$

Where the "E_{red}", "E^0_{red}", "R", "T", "n_e", "F", "$\mathrm{p}O_{2_{red}}$" and the "$\mathrm{p}O_{2_{ox}}$" represent the voltage measured in the sensor, the cell's potential in standard conditions, the ideal gas constant, the temperature, the number of transferred electrons in the reaction per molecule of oxygen (which as equation 28 shows is 4), the Faraday's constant (which is 96485,339924 $C.mol^{-1}$), the oxygen partial pressures outside with subscript ox (which is 0,21) and inside, subscript red, respectively.

5.2.3 The electrodes setup

The lower part of the present cell design contains the working, reference and counter electrodes. To study the electrochemical behavior of the anode, the difference of potential between the working and the reference electrodes would be measured over time. Between the working and the counter electrode, a current would be applied so that the electrons can be provided from the oxygen reduction reaction at the counter cathode producing O^{-2} ions that can travel through the YSZ electrolyte pellet to reach the working anode. Once in the working anode electrode, the oxide-ions can oxidize the molten alloy. Rhenium wire was used as the current collector for the working electrode in contact with this liquid environment.

5.2.4 Results of this experiments

The purpose of this experiment aimed to analyze the voltage behavior in the working anode along with the current passed through the system over the time. Regrettably, within a few hours of operation, all cell contacts showed very high resistances. This phenomenon occurred even a current was passed between working and counter electrodes. Moreover; it happened despite sealing under reducing conditions of flowing 10%H_2N_2. The cell was shut down and opened for observation and once it was dismantled and the inner sensor part container observation revealed no platinum wires in both pump and sensor parts (Figure 29).

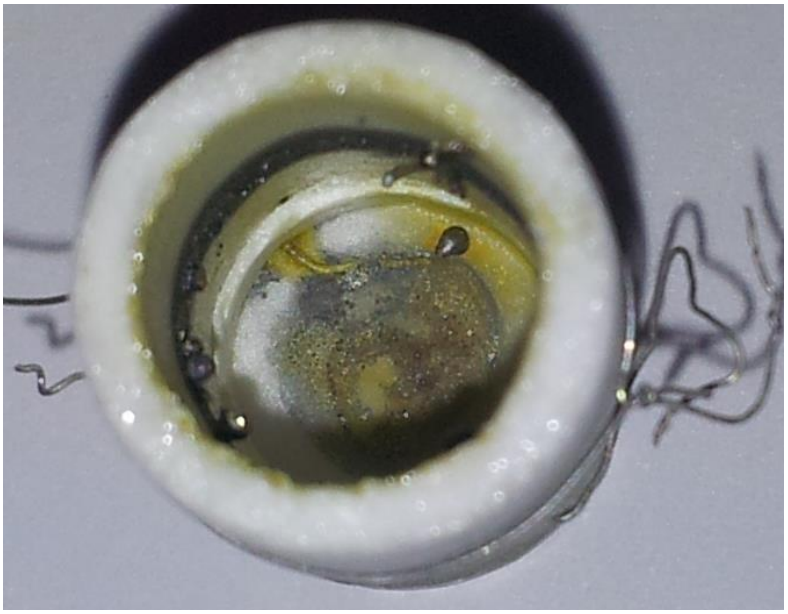

Figure 29 – Cell's sensor and pump after operation viewed from inside

This reaction between the platinum and the metals would be expected within the liquid metal if platinum wire was applied, as it can be predicted by the phase diagrams of both metals with platinum (Figure 30 and Figure 31). The existence of a liquid phase in both phase diagrams can justify why platinum wire cannot be applied within the liquid zone, however, reactions between platinum and gaseous metals in the sensor and pump inner part wires were unexpected.

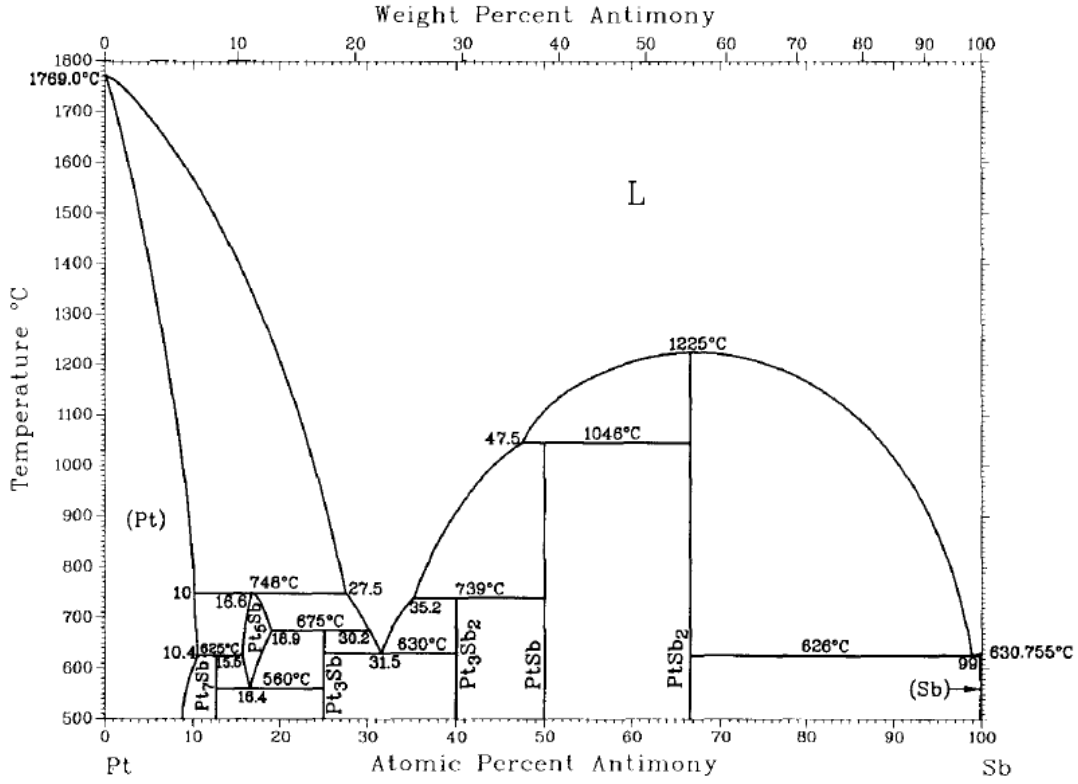

Figure 30 – Pt - Sb Phase diagram [29]

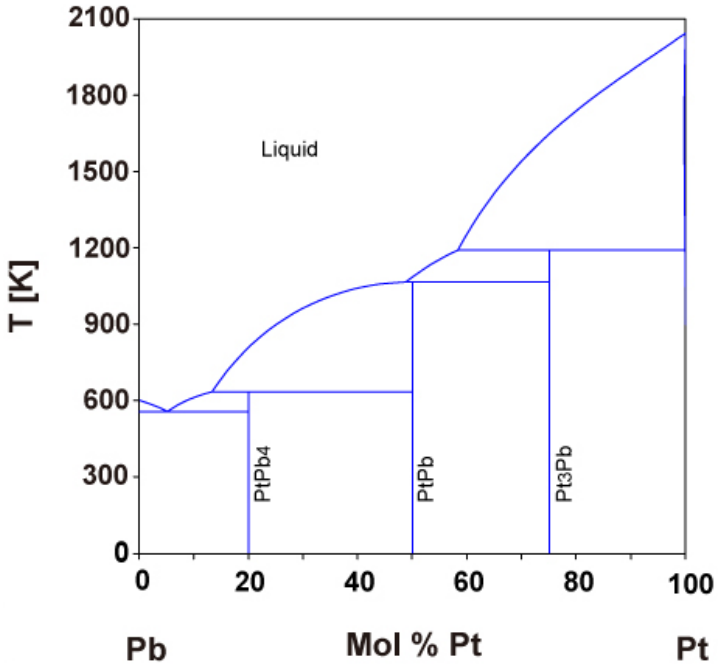

Figure 31 – Pb - Pt Phase diagram [30]

5.2.5 Conclusions of the first cell behaviour

To attempt to understand the observed results a crucible containing another smaller crucible with the metals in the same 1:1 ratio and a YSZ pellet with both platinum wire and paste (Figure 32) was prepared to be submitted to the cell's operation temperature under reducing conditions. The furnace temperature increased 4 °C per minute until it reached 700 °C, where it stood for 5 minutes, and from where it cooled down to environment temperature with a rate of 2 °C per minute. During the complete experiment, 1 nLiter per hour of 10%H_2/N_2 gas was in order to maintain reducing conditions.

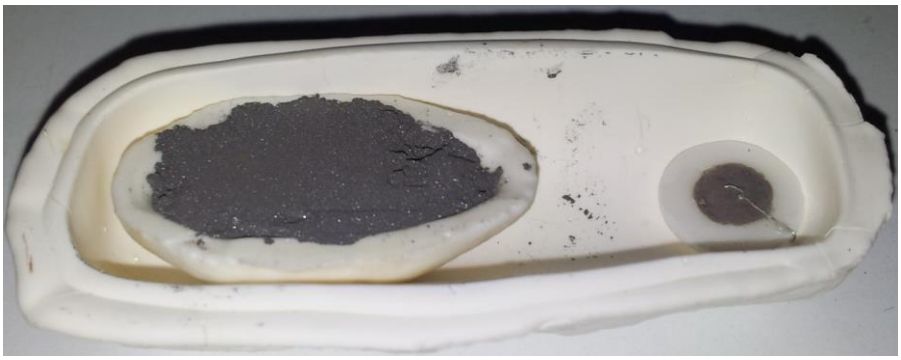

Figure 32 – Crucible with metals and platinum before experiment

Once cooled down, the crucible was carefully removed from the furnace and its observation provided useful information as it once again highlighted reaction between the reduced gas metals and the platinum wire and paste in the pellet (Figure 33). No platinum wire was observed after the experiment, instead, similar metallic balls to the ones in the inner part of the

sensor were found in the YSZ pellet. This strengthens the existence hypothesis of a reaction between the platinum and the metals in gaseous form due to volatilization of the metals even in their reduced state.

Figure 33 – Crucible with metals and platinum after experiment

5.3 Second cell project (without contact between platinum and metals)

As the previous 5.2 part of this chapter shows, the metals in the gaseous phase react in contact with platinum, therefore a new cell model was created in order to overcome this obstacle (Figure 34). However, regardless of the efforts made with this new design, the experiment found several difficulties in respect to the matter of sealing due to leaving at high temperature during the night before measurement.

The oxygen sensor voltage (which is the potential difference between the numbers 6 and 7 in Figure 34) revealed an oscillating behavior (Figure 35). The same behavior was detected too in the anode compartment and was again detected through the observation of oscillation (Figure 36) in the potential difference measured between the sensor and working electrodes (which are represented in Figure 34 by the numbers 3 and 4 respectively).

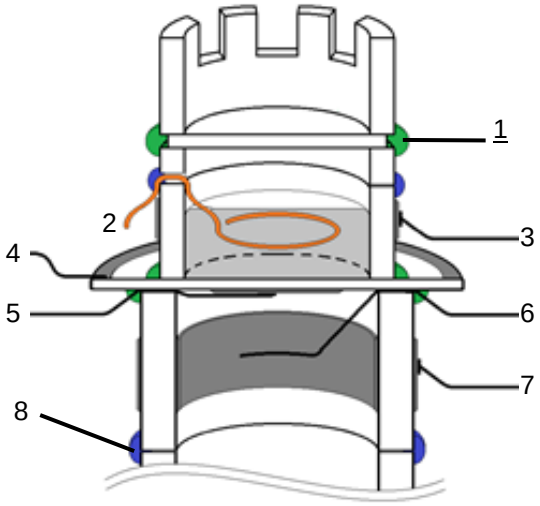

Legend:
1 – High temperature sealing glass (1195 °C), **2** – Rhenium wire of working electrode, **3** – Sensor
4 – Reference electrode, **5** – Counter electrode, **6** – Inner Oxygen sensor
7 – Outer Oxygen sensor, **8** – Low temperature sealing glass (900 °C)

Figure 34 – The second closed container cell design

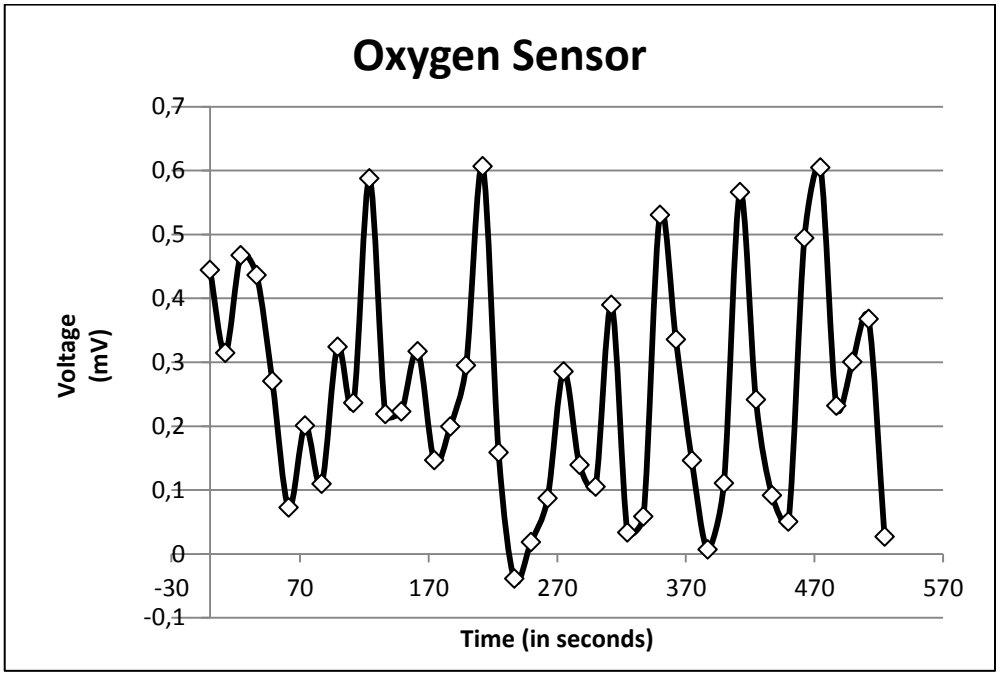

Figure 35 –Potential difference over time at constant temperature of 706 °C in the oxygen sensor

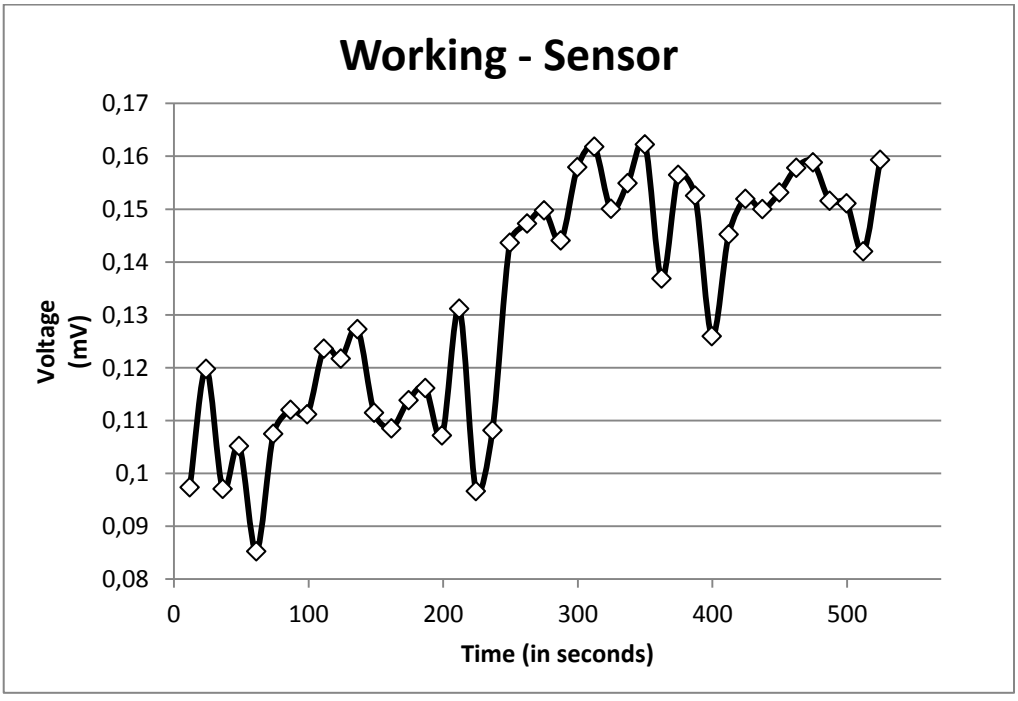

Figure 36 –Potential difference over time at constant temperature of 706 °C between working and sensor electrodes

The cell was shut down and opened for observation (Figure 37). The oscillating voltage profiles were clearly caused by leaking seals. The glass itself changed its color around the cell (from the common white to brown), suggesting that the long exposure to the sealing conditions

might promote a reaction between the sealing glass and the metal and the presence of molten metal outside of the container can also be observed due to leakage to the molten metal through the glass seal.

Figure 37 – Second closed container cell after the experiment

Another important detail noticed in the cell's observation after the experiment was the Rhenium wire absence in the outside part of the cell (Figure 38). This intriguing event led to further investigation, and after a quick search it was found that the rhenium oxide sublimes at only 360°C. Despite the reported stability of rhenium metal in reducing conditions to these melts [31] any oxidation of the rhenium wire leads it to sublime. Thus, one is forced to perform the final sealing procedure under reducing conditions of the upper seal.

Figure 38 – Second closed container cell after the experiment seen from the angle of the outside missing Rhenium wire

From these results, some factors were taken into consideration in the next cell design. To avoid rhenium sublimation upon oxidation, the sealing of the next cell should run under reducing

conditions. However, the next sections show that sealing using glass seals under reducing conditions was very difficult.

5.3.1 First attempt to determine the melting point temperature in reducing conditions

To try to find out the correct temperature of the glass melting point in a reducing atmosphere, a thin line of glass powder was dispersed in a long tubular crucible, from some centimeters aside of the center (marked with an arrow in Figure 39) to the other side. This crucible was then placed in a tubular furnace of known temperature profile. In this way, the correct melting glass position will reveal the correct melting temperature to use in these conditions once compared with the furnace temperature profile. Once the (10% H_2 and 90% N_2) gas mixture circulated for 30 minutes with 2 nL per hour flow, the furnace was heated up at 5°C.min^{-1} up to 900°C, where it stood for 20 minutes.

Figure 39 – Glass line before sealing procedure

After the sealing procedure was complete, the glass line was removed from the furnace (Figure 40) and contrary to what expected the glass did not melt even in the region closer to the central hot zone. Moreover, the dark color suggests a reaction between some of the glass components and the gas might have happened. In spite of this hypothesis, a new experiment took place in order to find the glass melting point at higher temperature.

Figure 40 – Glass line after sealing procedure

5.3.2 Second attempt to determine the melting point temperature in reducing conditions

Like described in the previous section, a picture of the line glass was taken before the sealing conditions period befell (Figure 41).The same procedure was repeated, but since the glass did not melt in the first attempt, the furnace temperature was then increased from 900°C to 950°C. The glass line holder was used this time in inverted position so that more glass is present around the center position of the furnace.

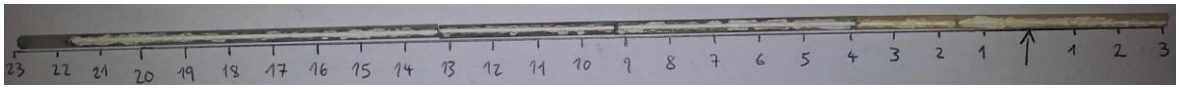

Figure 41 – Glass line before sealing (second attempt)

Regardless the efforts to find the melting point of the glass through the temperature increase, no melting zone was observed along the glass line after this second attempt (Figure 42). The melting point of the glass is superior to 950°C under reducing atmosphere. It was decided that such high temperatures would be unrealistic for the current experiment due to the associated higher risks of metal volatilization and inter-reaction with the surrounding components, e.g. crucibles/wires.

Figure 42 – Glass line after sealing (second attempt)

5.4 Third cell project (using new sealing material)

From the results of the last cell designs a new model was created. Except for the top seal (number 1 in Figure 43), all the other components were sealed together in air. Next, 3.0538 grams of the Pb:Sb molten alloy were introduced in the anode chamber. A different seal Thermiculite 866 was used to seal the anode under reducing conditions. This mass of alloy taken is expected to generate a high of 7.2259 millimeters of molten metal inside the anode container, which is enough to provide contact with the previously placed rhenium wire.

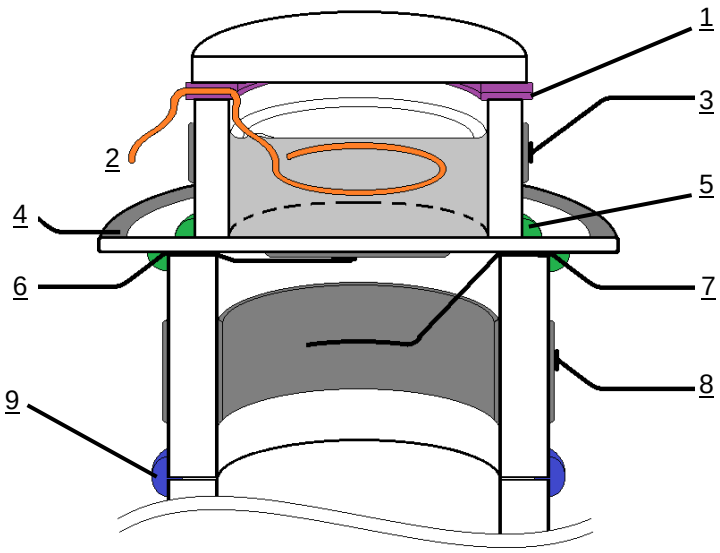

Legend:
1 – Thermiculite 866 (new sealant), **2** – Rhenium wire of working electrode, **3** – Sensor electrode
4 – Reference electrode, **5** – High temperature sealing glass (1195 °C)
6 – Counter electrode Platinum wire, **7** – Oxygen internal Platinum wire
8 – Oxygen external Platinum wire, **9** – Low temperature sealing glass (1115 °C)

Figure 43 – The third closed container design (with new sealant material)

Once the operation temperature of 700°C was stable, the initial conditions were registered many times. The difference of potential between the working electrode and the sensor varied from 370.65 to 384.23 millivolt. As for the potential difference between the working and reference electrodes, those fluctuate between 148.68 and 189.85 millivolt.

The diameter of the anode compartment was 9.2 mm and in order to obtain a current density value of 0.25 $A.cm^{-2}$, 53 mA were applied between the working and counter electrodes. With this current value stabilized, the voltages observed between the working electrode and the sensor as well as the working electrode and the reference were respectively in average 606 millivolt and 706 millivolt.

5.4.1 Oxygen-ions pumped through the third cell

In this section, the oxygen-ion moles pumped through the cell is compared with the theoretical value relative to total oxidation of the anode. The powder molar proportion is 1:1, so the number of moles of both metals is the same. From the atomic weight of each metal ($M_{Sb} = 121.76\ g.mol^{-1}; M_{Pb} = 207.2\ g.mol^{-1}$), the number of moles was determined ($n_{Pb} = n_{Sb} = 9.28 \times 10^{-3} mol$).

From the lead oxidation reaction (equation 30), each mole of metal requires exactly the same number of oxygen-ion moles to complete the oxidation. Yet, each mole of antimony metal demands 1.5 moles of oxygen-ions (equation 31), making so that the total oxygen ion number of moles to obtain 100% of oxidation is $23.21 \times 10^{-3} mol$.

$$2Pb + O_2 -> 2PbO \quad (30)$$

$$4Sb + 3O_2 -> 2Sb_2O_3 \quad (31)$$

Oxygen was pumped during 12 hours, but after 3 hours of operation a serious drop in the current values was registered (Figure 44). Notwithstanding, the current values registered over the time were used (in (7) to determine the total number of oxygen ion moles pumped to the anode ($3.02 \times 10^{-3} mol$) and this value corresponds to 13% of total oxidation before the current drop.

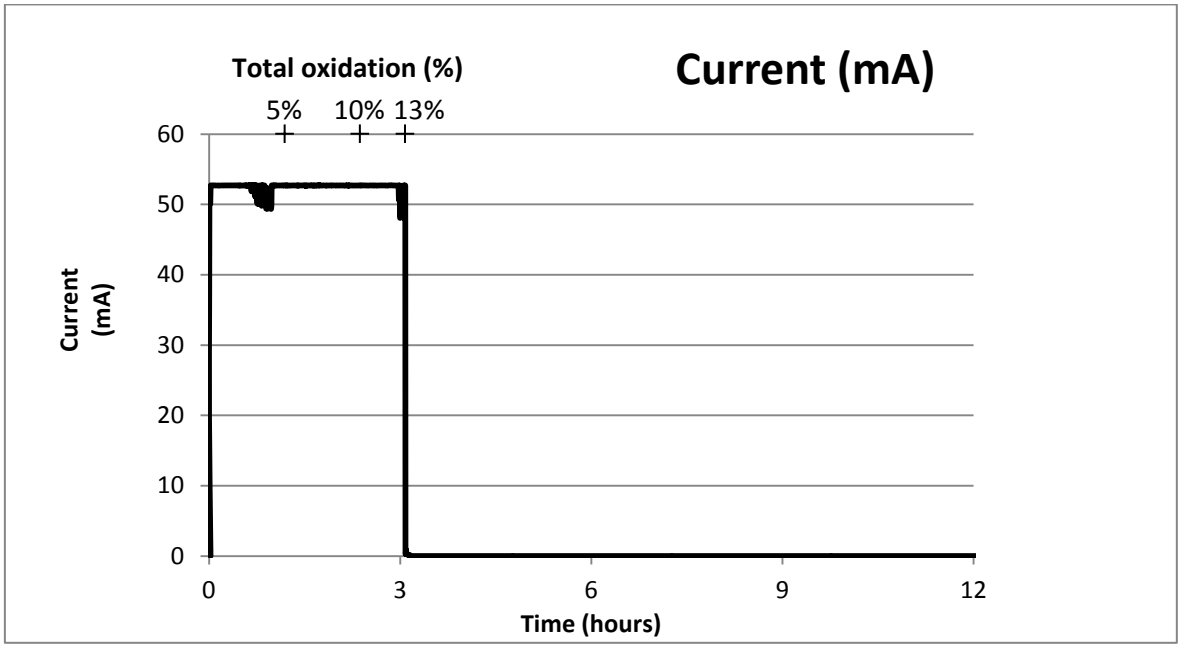

Figure 44 – Current drop after 3 hours of operation

5.4.2 Voltage degradation

The difference of potential between working and reference (Figure 45) and between working and sensor (Figure 46) seemed stable after the first hour of experiment. However, these values soon attain the setpoint for limiting potential ascribed to the experiment. On subsequent examination all platinum wires on the outside of the cell had melted, Figure 47. Possible reasons for this result may be that the internal pressure of the cell might have increased too much due to Sb_2O_3 volatilization for the sealant materials to continue to provide a seal or possible seal failure due a chemical reaction between the metal and one of the sealants, as shown in Figure 37, might

have occurred to produce a leak of antimony oxide to the 10%H_2/N_2 gas mixture outside the anode. In contact with this gas mixture the antimony oxide would be reduced to Sb, reacting with the outer wires of platinum. The result of these effects lead to the breakage of the platinum contact to the working electrode and short circuiting of this wire onto the reference electrode (Figure 47) disabling any chances to continue our experiment.

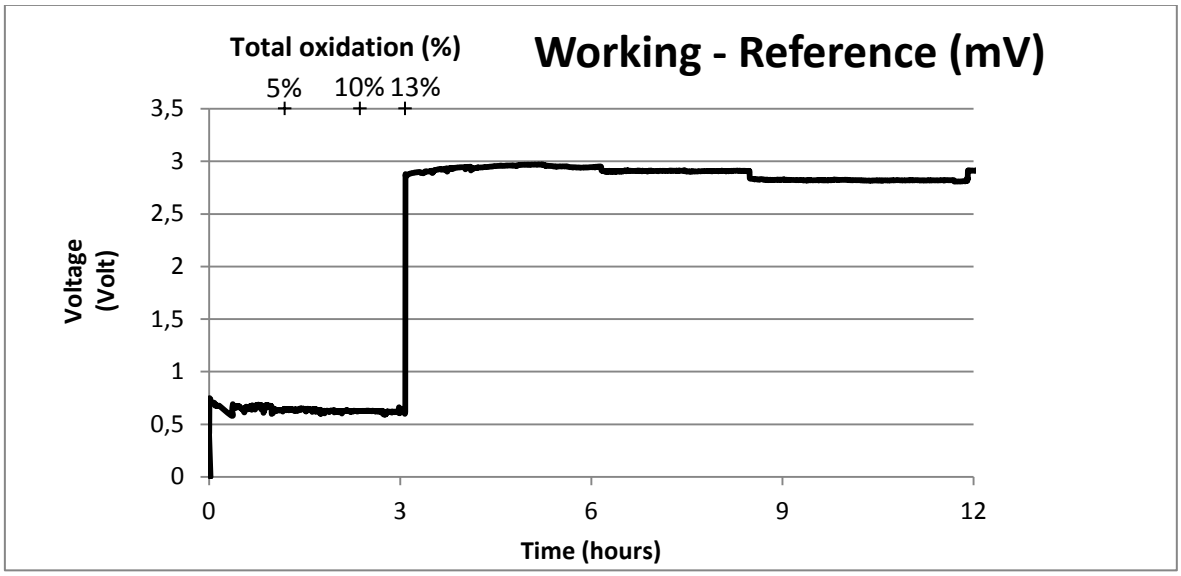

Figure 45 – Voltage measurement between working and reference electrodes

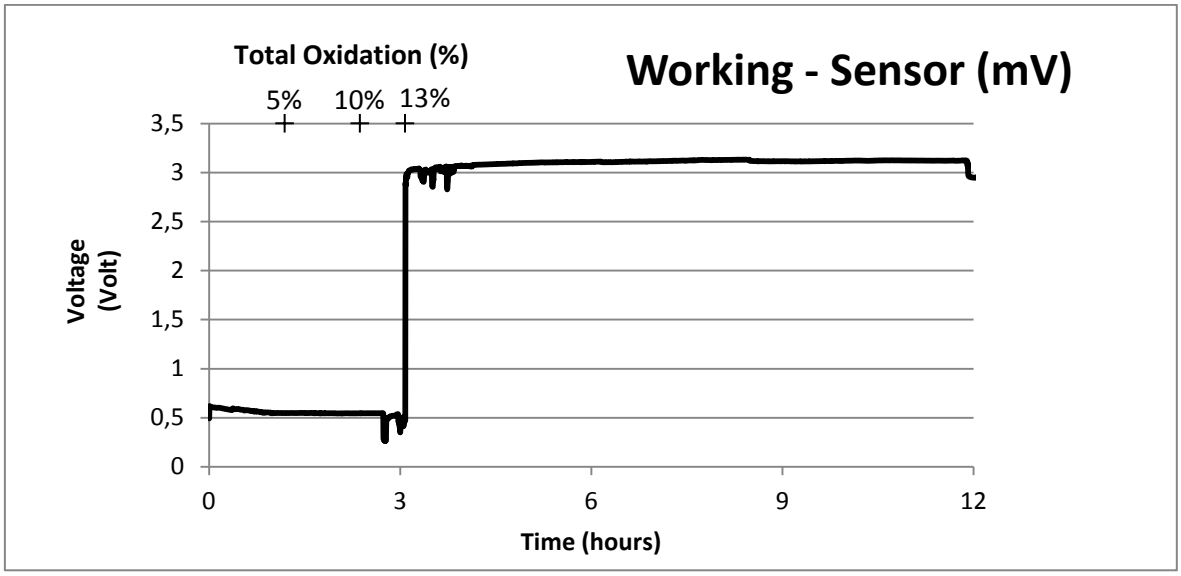

Figure 46 – Voltage measurement between working and sensor electrodes

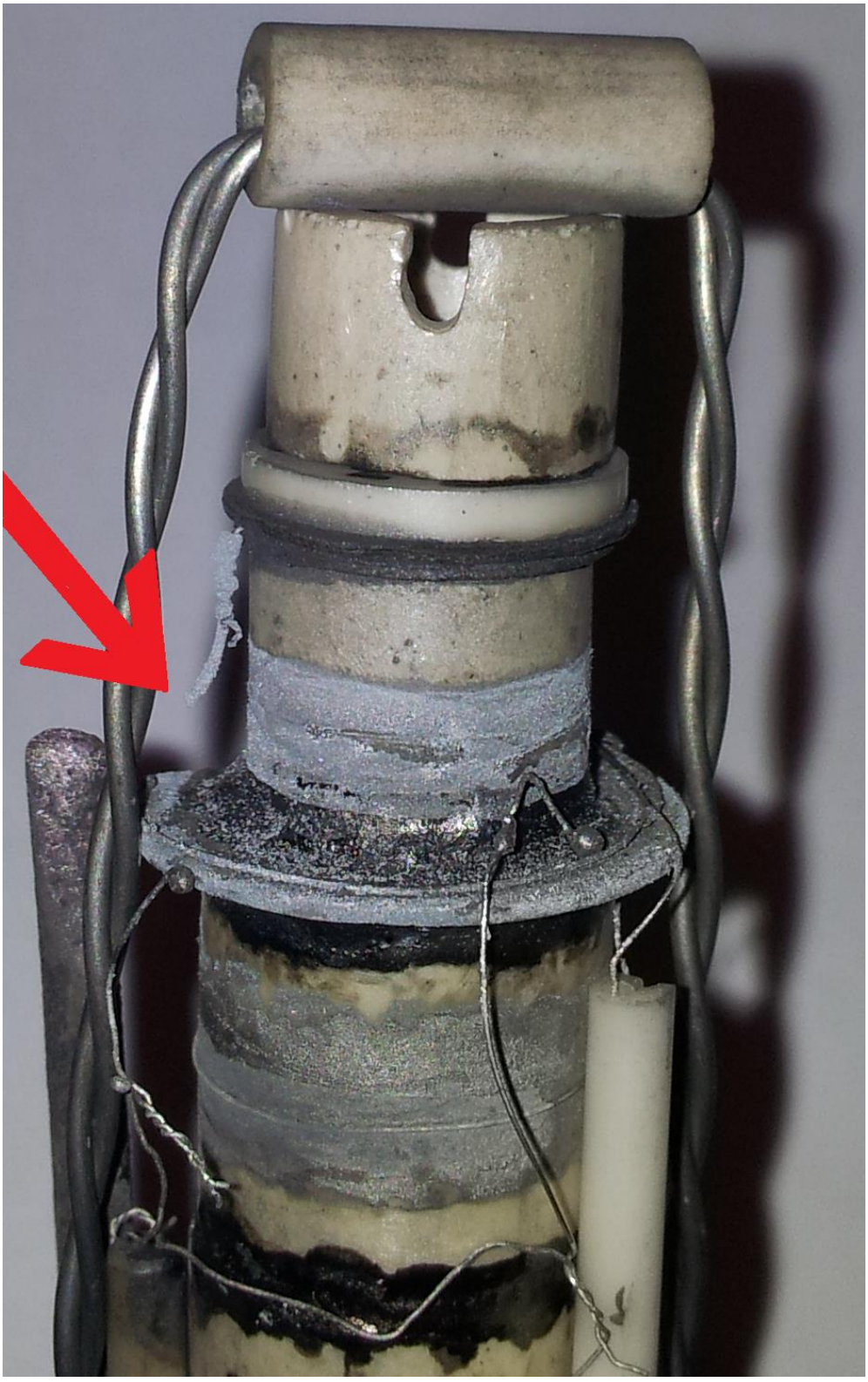

Figure 47 – Working electrode broken wire

Chapter 6 – Conclusions and future work

Many criteria were applied to choose the potential metal alloys (such as melting point, operation gap, congruent melting, oxides and pure metals phase diagrams comparison and Ellingham diagram analysis). From these criteria, five oxide binary systems were highlighted as possible anode candidates (which were $PbO\text{-}Sb_2O_3$, $GeO_2\text{-}PbO$, $Bi_2O3\text{-}CuO$, $Bi_2O_3\text{-}PdO$ and $Bi_2O_3\text{-}GeO_2$). Among these five, the system $PbO\text{-}Sb_2O_3$ was selected because it provided the cheapest solution once the price analysis took place (in the section 2.4 of the second chapter). Through this work it was found that new criteria should also be added to the methodology. Very importantly, the alloy vapour pressure, and possible reactions with the cell sealants or with the contact wires should be added as new criteria to be pre-analysed in future studies.

Within this chosen alloy, the vapour pressure was found to be a very pertinent detail because it complicated the option of using an opened container cell due to compositional drift. This way, it was concluded that the closed container was the best option to be able to study the electrochemical behaviour of this anode system with the provided equipment. This conclusion led to the volatilization calculation study and the later cell designs that took this important factor into consideration during the creation process. The vapour pressure differences along with the temperature found between the oxides and the pure metals (in section 4.3) revealed the antimony tendency to volatilize itself before the cell's operation temperature is reached. This led to the outcome of starting from reduced metals and later provoke the oxidation through pumping oxygen to a closed anode compartment.

The reaction between platinum and the alloy must be analysed and avoided by consultation with the respective phase diagrams before running the cell. This suggests a change in the experimental used methodology in the way that before using any substance as any fuel cell component, the materials should be assessed individually in every possible combination under all relevant conditions. Similar analysis must be applied to potential reactions between the sealing glass and the metal alloy and possible sublimation on oxidation of the contact wires, e.g. the rhenium wire sublimation event under oxidizing conditions. In spite of being very stable under reducing conditions, in air atmosphere, once the temperature increases, the rhenium turns into rhenium oxide and sublimes. Despite the occurrence of reactions between components, such materials may possibly be used if suitable cell design and preparation order is adopted. Several different cell designs were suggested for this goal and initial measurements could be taken, However, further effort needs to be implemented in this aim to address over-pressure and long term stability issues that are still shown to limit testing.

It is still unknown if the single phase oxide compound, $PbO\text{-}Sb_2O_3$, as a fuel cell anode can offer benefit over the composition $PbO\text{-}1/2Sb_2O_3$. This main question cannot be answered until this substance is sealed successfully and submitted in a working cell for a longer period of time (with contact between the cells electrodes and the sample holder outlets) so that the proper data can be acquired to discuss the viability of this material. After all the relevant data is obtained and properly saved for further analysis and discussion, the cell should be opened for observation, and if possible, further analysis to make sure no component reactions occurred to influence the obtained data.

Several issues came up within this study of the electrochemical behaviour of a candidate for a SOFC anode. In order to overcome these obstacles, some modifications can be implemented in the components of the system that are susceptible to change with the available technology.

Since the experiment suffered greatly from contact wire reactions, e.g. Pt reaction with the target alloy, or sublimation of Re on oxidation, in future work, the suggestion of different wire materials should be investigated. For example, high temperature alloys could be used. Separate experiments to assess the stability of the glass seals with the alloys should be performed. Further designs to limit the number of seals, for example, the use of closed end working tubes can also be considered. A new cell designs should be careful assessed before operation for potential inter-reactions or failures, and the order of sealing and cell building should be carefully planned with respect to the materials chosen. Finally the other potential alloy combinations highlighted in the work, $PbO\text{-}Sb_2O_3$, $GeO_2\text{-}PbO$, $Bi_2O3\text{-}CuO$, $Bi_2O_3\text{-}PdO$ and $Bi_2O_3\text{-}GeO_2$, should be studied after theoretical analysis of the other criteria such as vapour pressure, possible reactions with sealant materials and contact wires.

Bibliography

[1] - BP Energy Outlook 2035. (2014).

[2] - Público. (2014). Retrieved June 9, 2014, from http://www.publico.pt/ecosfera/noticia/quase-60-da-electricidade-consumida-em-2013-foi-renovavel-1619592#/0

[3] - Richter, J., Holtappels, P., Graule, T., Nakamura, T., & Gauckler, L. J. (2009). Materials design for perovskite SOFC cathodes. *Monatshefte Für Chemie - Chemical Monthly*, *140*(9), 985–999. doi:10.1007/s00706-009-0153-3

[4] - Aguiar, P., Lapen, N., Chadwick, D., & Kershenbaum, L. (2001). Improving catalyst structures and reactor con " gurations for autothermal reaction systems : application to solid oxide fuel cells, *56*, 651–658.

[5] - Fergus, J. W. (2006). Electrolytes for solid oxide fuel cells. *Journal of Power Sources*, *162*(1), 30–40. doi:10.1016/j.jpowsour.2006.06.062

[6] - Bove, R. (2004). 11 . Solid Oxide Fuel Cells : Principles , Designs and State-of-the-Art in Industries.

[7] - Basu, R. N. (2004). 12 . Materials for Solid Oxide Fuel Cells.

[8] - Sun, C., Hui, R., & Roller, J. (2009). Cathode materials for solid oxide fuel cells: a review. *Journal of Solid State Electrochemistry*, *14*(7), 1125–1144. doi:10.1007/s10008-009-0932-0

[9] - Boukamp, B. A. (2003). Fuel cells: The amazing perovskite anode. *Nature Materials*, 294–296. doi:10.1038/nmat892

[10] - Qiu, L., Ichikawa, T., Hirano, A., Imanishi, N., & Takeda, Y. (2003). $Ln_{1-x}Sr_xCo_{1-y}Fe_yO_{3-\delta}$ (Ln=Pr, Nd, Gd; x=0.2, 0.3) for the electrodes of solid oxide fuel cells, *158*, 55–65.

[11] - Laosiripojana, N., Wiyaratn, W., Kiatkittipong, W., Arpornwichanop, A., Soottitantawat, A., & Assabumrungrat, S. (2009). Reviews on Solid Oxide Fuel Cell Technology. *Engineering Journal*, *13*(1), 65–84. doi:10.4186/ej.2009.13.1.65

[12] - Zhu, W. ., & Deevi, S. . (2003). A review on the status of anode materials for solid oxide fuel cells. *Materials Science and Engineering: A*, *362*(1-2), 228–239. doi:10.1016/S0921-5093(03)00620-8

[13] - Al-Salem, S. M., Lettieri, P., & Baeyens, J. (2009). Recycling and recovery routes of plastic solid waste (PSW): a review. *Waste Management (New York, N.Y.)*, *29*(10), 2625–43. doi:10.1016/j.wasman.2009.06.004

[14] - End-of-waste criteria for waste plastic for convertion: Technical proposals. (2011).

[15] - Hopewell, J., Dvorak, R., & Kosior, E. (2009). Plastics recycling: challenges and opportunities. *Philosophical Transactions of the Royal Society of London. Series B, Biological Sciences*, *364*(1526), 2115–26. doi:10.1098/rstb.2008.0311

[16] – European commission DG ENV. (2011). *PLASTIC WASTE IN THE ENVIRONMENT - Final Report*.

[17] - World production of Municipal Solid Waste (MSW),. (2012), 16–17. Retrieved from http://www.proparco.fr/jahia/webdav/site/proparco/shared/PORTAILS/Secteur_prive_developpement/PDF/SPD15/SPD15_key_data_uk.pdf

[18] - Jayakumar, a., Lee, S., Hornés, a., Vohs, J. M., & Gorte, R. J. (2010). A Comparison of Molten Sn and Bi for Solid Oxide Fuel Cell Anodes. *Journal of The Electrochemical Society*, *157*(3), B365. doi:10.1149/1.3282443

[19] - Jayakumar, a., Vohs, J. M., & Gorte, R. J. (2010). Molten-Metal Electrodes for Solid Oxide Fuel Cells. *Industrial & Engineering Chemistry Research*, *49*(21), 10237–10241. doi:10.1021/ie100457t

[20] - Javadekar, A., Jayakumar, A., Pujara, R., Vohs, J. M., & Gorte, R. J. (2012). Molten silver as a direct carbon fuel cell anode. *Journal of Power Sources*, *214*, 239–243. doi:10.1016/j.jpowsour.2012.04.096

[21] - Javadekar, A., Jayakumar, A., Gorte, R. J., Vohs, J. M., & Buttrey, D. J. (2011). Characteristics of Molten Alloys as Anodes in Solid Oxide Fuel Cells. *Journal of The Electrochemical Society*, *158*(12), B1472. doi:10.1149/2.006112jes

[22] - The interactive Ellingham diagram. (n.d.). Retrieved January 15, 2014, from http://www.doitpoms.ac.uk/tlplib/ellingham_diagrams/interactive.php

[23] - Thermfact and GTT-Technologies. (n.d.). FactSage 6.2. FactSage (TM) - Copyright (C).

[24] - ACerS and NIST. (1964). Phase diagrams for ceramists. In *Vol. 1, 2, 3, 4, 6, 8, 11 and 12*.

[25] - Sigma Aldrich. (2014). Retrieved January 25, 2014, from http://www.sigmaaldrich.com/portugal.html

[26] - M. Kopyto, W. Przybylo, B. Onderka, K. F. (2009). Thermodynamic properties of Sb_2O_3-SiO_2 and PbO-Sb_2O_3-SiO_2 liquid solutions. *Archives of Metallurgy and Metals*, *54*(3).

[27] - Pere, F., Constantin, I., & Among, I. (2010). THERMODYNAMIC STUDY OF BINARY Pb-Sb SYSTEM USING THE POSS MODEL, *72*.

[28] - Wang, L., Wang, Q., Xian, a, & Lu, K. (2007). Precise measurement of the densities of liquid Bi, Sn, Pb and Sb. *Journal of Physics: Condensed Matter*, *19*(13), 139001. doi:10.1088/0953-8984/19/13/139001

[29] - Okamoto, H. (1992). Pt-Sb (platinum-antimony). *Journal of Phase Equilibria*, *13*(5), 580–581. doi:10.1007/BF02665778

[30] - Long, Z. H., Tao, X. M., Liu, H. S., & Jin, Z. P. (2009). Calculated Pb-Pt phase diagram assessed by 2009Lon. *J. Phase Equ.Diff. 30*. Retrieved March 25, 2014, from http://www.nims.go.jp/cmsc/pst/database/pb-elem/pbpt/pbpt.htm

[31] - Greenwood, N. N., & Earnshaw, A. (1997). *Chemistry of the Elements*.